A Multistructure Multimode Three-Phase Dual-Active-Bridge Converter Targeting Wide-Range High-Efficiency Performance

Akif Zia Khan, *Student Member, IEEE*, Yiu Pang Chan, *Student Member, IEEE*, Muhammad Yaqoob, *Member, IEEE*, Ka-Hong Loo, *Member, IEEE*, Pooya Davari, *Senior Member, IEEE*, and Frede Blaabjerg, *Fellow, IEEE*

***Abstract*—A three-phase dual-active-bridge (3p-DAB) converter is an attractive topology for bidirectional power conversion in high-power applications. However, conduction and switching losses are two main loss mechanisms that severely affect its efficiency performance, and adoption of any single modulation scheme or topology cannot minimize these losses over a wide operating range. For this purpose, a reconfigurable topology of the 3p-DAB converter is proposed in this article that utilizes a reconfigurable and tunable resonant network to offer multiple degrees of freedom in minimizing conduction and switching losses over a wide range of operating conditions. The converter is designed such that for 40–100% of the rated output power, it operates as a tunable 3p-DAB resonant immittance converter with its output power controlled by varying switching frequency and tuning the resonant frequency of a resonant immittance network to track the switching frequency. Below 40% of the rated output power, the converter transforms to a tunable 3p-DAB series-resonant converter with its output power controlled by varying the impedance of a series-resonant network while keeping the switching frequency and phase shift constant. The combination of both operation modes jointly leads to wide-range zero circulating current and soft switching of all the switches and, hence, a wide-range high-efficiency performance, as validated by the experimental results.**

***Index Terms*—DC–DC power conversion, immittance converters (ICs), resonant power conversion, series-resonant network, unity power factor (UPF), zero-voltage switching (ZVS).**

NOMENCLATURE

3p-DAB	Three-phase dual active bridge.
ZVS	Zero-voltage switching.
SPS	Single phase shift.
DoF	Degree of freedom.
rms	Root mean square.
DABRIC	Dual-active-bridge resonant immittance converter.
DABSRC	Dual-active-bridge series-resonant converter.
RTRN	Reconfigurable and tunable resonant network.
TRIN	Tunable resonant immittance network.
TSRN	Tunable series-resonant network.
SCC	Switch-controlled capacitor.
DFM	Dynamic frequency matching.
D_{p}	Duty cycle of switches in the primary bridge.
D_{s}	Duty cycle of switches in the secondary bridge.
θ	Phase shift between primary-bridge and secondary-bridge ac voltages.
ψ	Control angle of the SCC.
ϕ	Phase angle of port currents.
f_{s}	Switching frequency.
$f_{\mathrm{s,max}}$	Maximum switching frequency.
$f_{\mathrm{s,min}}$	Minimum switching frequency.
$\mathbf{X_A}$	Capacitive impedance comprising L_1 and C_1.
$\mathbf{X_B}$	Inductive impedance comprising L_2 and C_2.
ω_{a}	Angular series resonance frequency of L_1 and C_1.
ω_{b}	Angular series resonance frequency of L_2 and C_2.
ω_{s}	Angular switching frequency.
ω_{r}	Angular resonance frequency of $\mathbf{X_A}$ and $\mathbf{X_B}$.
$\omega_{\mathrm{r,max}}$	Maximum angular resonance frequency of $\mathbf{X_A}$ and $\mathbf{X_B}$.
$\omega_{\mathrm{r,min}}$	Minimum angular resonance frequency of $\mathbf{X_A}$ and $\mathbf{X_B}$.
$S_{\mathrm{N}x}$	Switches S_{N1}, S_{N2}, and S_{N3} in branch $\mathbf{X_A}$ used for transformation of network.
$S_{\mathrm{T}x\mathrm{A}}$	Switches S_{T1A}, S_{T2A}, and S_{T3A} in branch $\mathbf{X_B}$ used for tuning $C_{2\mathrm{t}}$.
$S_{\mathrm{T}x\mathrm{B}}$	Switches S_{T1B}, S_{T2B}, and S_{T3B} in branch $\mathbf{X_B}$ used for tuning $C_{2\mathrm{t}}$.
S_{j1}, S_{j2}	Complimentary switches in the primary-bridge where $j = \mathrm{A}, \mathrm{B}$, and C is used for phase designation.
Q_{j1}, Q_{j2}	Complimentary switches in the secondary-bridge where $j = \mathrm{A}, \mathrm{B}$, and C is used for phase designation.
$C_{2\mathrm{t}}$	Tunable capacitors comprising base capacitors C_2 and switches $S_{\mathrm{T}x\mathrm{A}}$ and $S_{\mathrm{T}x\mathrm{B}}$.
$P_{\mathrm{o,max}}$	Maximum output power of 3p-DABRIC.

Manuscript received December 18, 2019; revised March 31, 2020 and June 16, 2020; accepted August 4, 2020. Date of publication August 6, 2020; date of current version October 30, 2020. This work was supported by the Hong Kong Polytechnic University Central Research under Grant G-YBXL. Recommended for publication by Associate Editor S. Choi. *(Corresponding author: Akif Zia Khan.)*

Akif Zia Khan, Yiu Pang Chan, and Ka-Hong Loo are with the Department of Electronic and Information Engineering, The Hong Kong Polytechnic University, Hung Hom, Hong Kong (e-mail: akifzia.khan@connect.polyu.hk; yiu-pang.yp.chan@connect.polyu.hk; kh.loo@polyu.edu.hk).

Muhammad Yaqoob is with the Huawei Research Center, 16440 Stockholm, Sweden (e-mail: muhammad.yaqoob@connect.polyu.hk).

Pooya Davari and Frede Blaabjerg are with the Department of Energy Technology, Aalborg University, 9220 Aalborg, Denmark (e-mail: pda@et.aau.dk; fbl@et.aau.dk).

Color versions of one or more of the figures in this article are available online at https://ieeexplore.ieee.org.

Digital Object Identifier 10.1109/TPEL.2020.3014900

$P_{\mathrm{o,min}}$	Minimum output power of 3p-DABRIC.
$X_{\max}$	Maximum impedance of $\mathbf{X_A}$ and $\mathbf{X_B}$.
$X_{\min}$	Minimum impedance of $\mathbf{X_A}$ and $\mathbf{X_B}$.
n	Transformer's turn ratio.
V_{in}	DC input voltage of the converter.
V_{o}	DC output voltage of the converter.
G	Voltage ratio $nV_{\mathrm{o}}/V_{\mathrm{in}}$.
ϵ	Ratio of $P_{\mathrm{o,max}}$ to $P_{\mathrm{o,min}}$.
σ	Ratio of $f_{\mathrm{s,max}}$ to $f_{\mathrm{s,min}}$.
κ	Ratio of maximum $C_{2\mathrm{t}}$ to minimum $C_{2\mathrm{t}}$.

I. Introduction

A 3p-DAB converter has been widely researched over the past few decades due to its superiority over other bidirectional power converter topologies in terms of modularity, lower component stress, higher power density, smaller input and output current ripple, smaller size of filter elements, galvanic isolation, and inherent soft-switching operation [1] . Due to these advantages, the 3p-DAB converter has been successfully applied in many emerging high-power applications such as solid-state transformers, vehicle-to-grid operation, uninterruptible power supplies, and dc microgrids.

The conventional 3p-DAB converter comprises two three-phase half-bridges interfaced by a three-phase high-frequency isolation transformer. The simplest modulation scheme for the 3p-DAB converter is the SPS modulation, where two phase-shifted high-frequency ac voltages are applied across transformer's leakage inductances for power flow control. The power flows from the leading to lagging ac voltage, with the phase shift being used as a control variable to control the output power. However, SPS modulation suffers from the drawbacks of high circulating current and narrow ZVS range, which is sensitive to input-to-output voltage ratio and load conditions. This makes it extremely challenging to maintain a high-efficiency operation of an SPS-controlled 3p-DAB converter for applications where the input-to-output voltage ratio is prone to wide-range variations.

To overcome the drawbacks of SPS modulation, various modulation schemes have been proposed for the 3p-DAB converter that make use of additional DoFs for more efficient power flow control at the expense of increased control complexity. The control variables available for modulating the 3p-DAB converter are the duty cycles (D_{p}, D_{s}) of the complimentary switches in the primary and secondary bridges, phase shift (θ) between the primary-bridge and secondary-bridge ac voltages, and the switching frequency (f_{s}). Simultaneous control of two control variables gives rise to a two-DoF modulation scheme for the 3p-DAB converter. The most popular two-DoF modulation scheme reported for the 3p-DAB converter is the duty-cycle plus phase-shift modulation, where the complimentary switches in both active bridges are modulated simultaneously with the same duty cycle (i.e., $D_{\mathrm{p}} = D_{\mathrm{s}} = D$) in conjunction with the modulation of phase shift θ [2]–[5]. The advantages of this modulation scheme stem from its ability to generate and control the pulsewidth of the zero-voltage levels in the phase voltages (for the duty cycle range $0<D<1/3$) that can help minimize reactive power flow due to the zero-voltage levels and improve light-load efficiency. However, with reduced load (i.e., smaller values of D), the inductor current and energy flowing through the converter becomes increasingly discontinuous. Moreover, difficulty in the selection of optimal values of multiple control variables (D, θ) and high circulating current under heavy-load conditions are some of the drawbacks of this modulation scheme. Another two-DoF modulation scheme that utilized phase shift (θ) and switching frequency (f_{s}) as control variables to achieve a narrow frequency range for output power modulation and simplify closed-loop implementation was reported in [6] and [7]. However, the optimal efficiency performance of this modulation scheme remains highly sensitive to the input-to-output voltage ratio. To further enhance control flexibility, three-DoF modulation schemes that utilized three control variables D_{p}, D_{s}, and θ, where $D_{\mathrm{p}} \neq D_{\mathrm{s}}$, simultaneously for power flow control were proposed in [8] and [9]. These three-DoF modulation schemes were reported to achieve better performances in terms of reduced conduction loss and extended ZVS range [10]; however, they produce asymmetrical voltage waveforms that lead to increased reactive current flow. In addition, the extensive computational efforts involved in the optimization of three control variables D_{p}, D_{s}, and θ for different input-to-output voltage ratios render their implementation challenging.

In conjunction with the design of modulation schemes, another approach that has been widely researched for enhancing the efficiency of the 3p-DAB converter is based on topological variations. In this context, multilevel 3p-DAB converters have been widely investigated that offer the advantages of symmetrical voltage waveforms containing more voltage levels that help reduce reactive current flow as well as lower device stresses. For example, a T-type three-level 3p-DAB converter that was capable of producing a three-level ($+V_{\mathrm{DC}}/2$, 0, $-V_{\mathrm{DC}}/2$) symmetrical voltage waveform was proposed in [11]–[13]. The ability to control the duration of the zero-voltage state with this topology favors the minimization of reactive power flow and extension of ZVS range as compared to two-level ($+V_{\mathrm{DC}}/2$, $-V_{\mathrm{DC}}/2$) operation of the 3p-DAB converter. However, the issue of circulating current remains unsolved as the phase current continues to circulate in the converter during the zero-voltage state. For reducing the circulating current, a π-type four-level 3p-DAB converter was proposed in [14]. This topology was capable of producing a four-level ($+V_{\mathrm{DC}}/2$, $+V_{\mathrm{DC}}/6$, $-V_{\mathrm{DC}}/2$, $-V_{\mathrm{DC}}/6$) symmetrical voltage waveform leading to a more flexible output power control and wide-range zero circulating current. However, increased complexity and higher component count are some of the disadvantages of this topology. Another modified topology of the 3p-DAB converter was proposed in [15]–[17] that comprises three parallel 120° phase-shifted H-bridges at the primary side. This topology offers the freedom to utilize the internal phase shift between the two legs of the same H-bridge to generate a three-level ($+V_{\mathrm{DC}}$, 0, $-V_{\mathrm{DC}}$) symmetrical ac voltage with adjustable duty ratio. This topology was also proposed to limit reactive power flow and reduce conduction loss; however, it still failed to achieve wide-range ZVS operation. The concept of a modified auxiliary-resonant commutated pole was applied to the 3p-DAB converter in [18] to achieve wide-range ZVS

operation; however, conduction loss cannot be minimized using this approach.

In addition to different modulation schemes and multilevel topologies, resonant variants of the 3p-DAB converter have also been investigated extensively with the objective to enhance its efficiency performance. The insertion of different resonant networks to the high-frequency ac link of the 3p-DAB converter offers another DoF in achieving additional desirable characteristics such as dc-bias blocking capability, lower rms phase current, extended ZVS range, and unity-power-factor (UPF) operation [19]–[26]. For example, the series capacitor in a 3p-DAB series-resonant converter (3p-DABSRC) helps remove the dc bias in the phase current [27], [28]. Moreover, the sinusoidal current in the 3p-DABSRC gives rise to lower rms value as compared to the piecewise linear current in a nonresonant 3p-DAB converter, thus leading to a lower conduction loss. However, the conduction loss and ZVS operation of the 3p-DABSRC are still sensitive to the input-to-output voltage ratio. To achieve ZVS operation independent of the input-to-output voltage ratio, a 3p-DAB resonant immittance converter (3p-DABRIC) was proposed in [21], which enables a precise control of the phase current phasor and, thus, leads to full-range ZVS operation independently of the input-to-output voltage ratio. However, it suffers from severe circulating current under light-load conditions leading to poor light-load efficiency. A second mode of operation was proposed for the 3p-DABRIC in [21] to achieve an in-phase relationship between the voltages and currents at all ports of the immittance network, which leads to the elimination of reactive power and minimum conduction loss. However, 33% of the switches undergo hard switching in this mode of operation.

From the extensive literature review conducted, it can be concluded that it is very challenging, if not impossible, to achieve full-range ZVS operation and wide-range zero circulating current simultaneously with any one modulation scheme or topology of the 3p-DAB converter. This has motivated us to propose the idea of a reconfigurable topology and a modulation scheme that can dynamically adapt to varying operating conditions while ensuring that conduction and switching losses are minimized simultaneously over the whole operating range. To meet this objective, a reconfigurable topology of the 3p-DAB converter is proposed in this article that utilizes an RTRN for achieving a multiple DoF control of the 3p-DAB converter with the objective of maximizing its efficiency under widely varying operating conditions. The converter is designed such that from 40% to 100% of the rated output power, it operates as a tunable 3p-DABRIC with its output power controlled by varying the switching frequency and tuning the resonant frequency of the immittance network by means of an SCC. This gives rise to a UPF operation that eliminates all circulating current and reactive power flow. Moreover, all switches undergo ZVS independently of the input-to-output voltage ratio under this operation mode. This allows boosting the efficiency performance for medium-to-high output power levels. Below 40% of the rated output power, the converter transforms to a tunable 3p-DABSRC with its output power controlled by varying the impedance of a series-resonant network using SCC while keeping the switching frequency and phase shift at the optimal values as determined by the input-to-output voltage ratio. This operation mode ensures minimum-tank-current operation

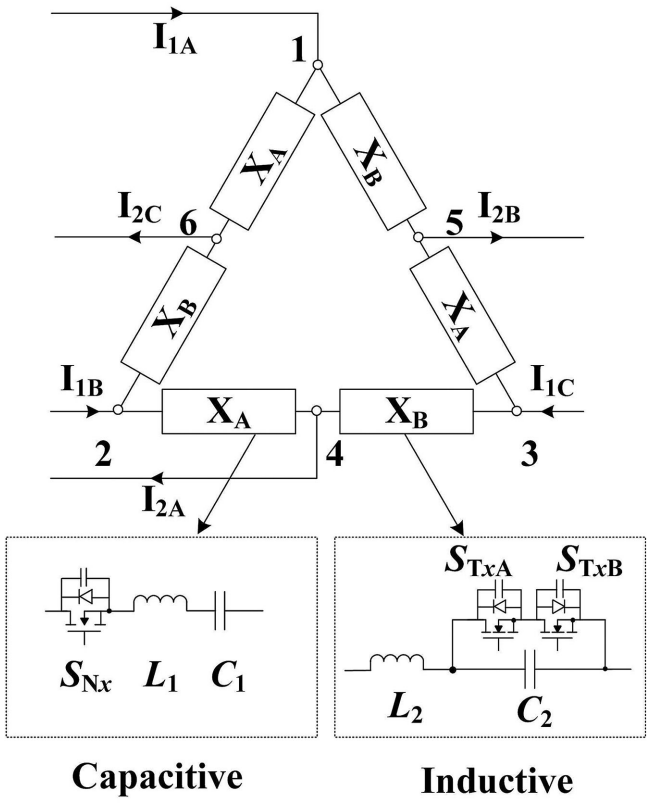

Fig. 1. Proposed RTRN.

that minimizes conduction loss, and full-range ZVS operation is achieved for all switches leading to enhanced efficiency performance for low-to-medium output power levels. The combination of both operation modes, therefore, leads to a wide-range high-efficiency performance of the proposed converter by minimizing both switching and conduction losses simultaneously.

The rest of this article is organized as follows. Section II introduces the proposed three-phase reconfigurable and tunable resonant network (3p-RTRN). The proposed 3p-DAB topology is discussed in Section III. The modeling and analysis of the two operating modes of the proposed 3p-DAB topology, namely, 3p-DABRIC and 3p-DABSRC, are discussed in Sections IV and V, respectively. The prototype design and experimental results are discussed in Section VI. Finally, Section VII concludes this article.

II. Proposed 3p-RTRN

The proposed 3p-RTRN is a delta-connected network consisting of two types of impedances labeled as $\mathbf{X_A}$ and $\mathbf{X_B}$, as shown in Fig. 1. $\mathbf{X_A}$ consists of switch $S_{\mathrm{N}x}$, inductor L_1, and capacitor C_1, whereas $\mathbf{X_B}$ consists of inductor L_2, capacitor C_2, and switches $S_{\mathrm{T}x\mathrm{A}}$ and $S_{\mathrm{T}x\mathrm{B}}$ (where $x = 1$, 2, and 3). $\mathbf{X_A}$ is constrained to operate below the series resonance frequency ω_{a} of L_1 and C_1, i.e., $\omega_{\mathrm{a}} > \omega_{\mathrm{s}}$, to constitute an overall capacitive impedance. On the contrary, $\mathbf{X_B}$ is constrained to operate above the series resonance frequency ω_{b} of L_2 and C_2, i.e., $\omega_{\mathrm{b}} < \omega_{\mathrm{s}}$, to constitute an overall inductive impedance. The switches $S_{\mathrm{N}x}$ in $\mathbf{X_A}$ are used to connect or isolate the capacitive impedance $\mathbf{X_A}$ from the network, thus enabling the transformation of the

network into different configurations. It should be noted that $\mathbf{X_A}$ can be fully isolated using only a two-quadrant switch as the body diode of $S_{\mathrm{N}x}$ is kept in a reverse biased stated by the voltage across C_1 when $S_{\mathrm{N}x}$ are turned OFF.

The switches $S_{\mathrm{T}x\mathrm{A}}$ and $S_{\mathrm{T}x\mathrm{B}}$ in $\mathbf{X_B}$ are used to electronically control the capacitance of C_2, thus enabling the control of the series impedance and tuning of the resonance frequency ω_{b} of L_2 and C_2. Regarding the labeling of the network terminals shown in Fig. 1, the following conventions are adopted: terminals 1–3 represent the input ports of the network, whereas terminals 4–6 represent the output ports of the network. Furthermore, subscripts $1j$ (where j = A, B, and C) are used to denote the parameters (e.g., line currents) at the input ports of the network, whereas subscripts $2j$ (where j = A, B, and C) are used to denote the parameters (e.g., line currents) at the output ports of the network.

Depending upon the state of switches $S_{\mathrm{N}x}$, $S_{\mathrm{T}x\mathrm{A}}$, and $S_{\mathrm{T}x\mathrm{B}}$, the 3p-RTRN can transform between three different network configurations. The configuration of Fig. 2(a) is obtained when $S_{\mathrm{N}x}$ are turned ON. This action connects the capacitive impedance $\mathbf{X_A}$ to the network and thus transforms the network to a three-phase tunable resonant immittance network (3p-TRIN). To simplify the drawing, $S_{\mathrm{N}x}$ are not shown in Fig. 2(a), whereas $S_{\mathrm{T}x\mathrm{A}}$, $S_{\mathrm{T}x\mathrm{B}}$, and C_2 are represented by a tunable capacitor $C_{2\mathrm{t}}$. The configuration of Fig. 2(b) is obtained when $S_{\mathrm{N}x}$ are turned OFF. This action isolates $\mathbf{X_A}$ from the network and thus transforms the network to a three-phase tunable series-resonant network (3p-TSRN). The third configuration shown in Fig. 2(c) is obtained by turning $S_{\mathrm{N}x}$ OFF and turning $S_{\mathrm{T}x\mathrm{A}}$/$S_{\mathrm{T}x\mathrm{B}}$ ON. This action isolates $\mathbf{X_A}$ from the network and bypasses C_2 in $\mathbf{X_B}$. In doing so, the network transforms to a conventional three-phase series inductor network.

The reconfigurability of the proposed network highlights the flexibility that it offers to the power control of the 3p-DAB converter. Since the 3p-TRIN and the 3p-TSRN offer the desirable characteristics of dc-bias blocking capability, lower rms phase current, full-range ZVS, and UPF operation, the scope of the present work is confined to the tunable resonant networks. The subsequent sections will discuss in detail the application of the 3p-TRIN and the 3p-TSRN in the 3p-DAB converter for improving its efficiency performance.

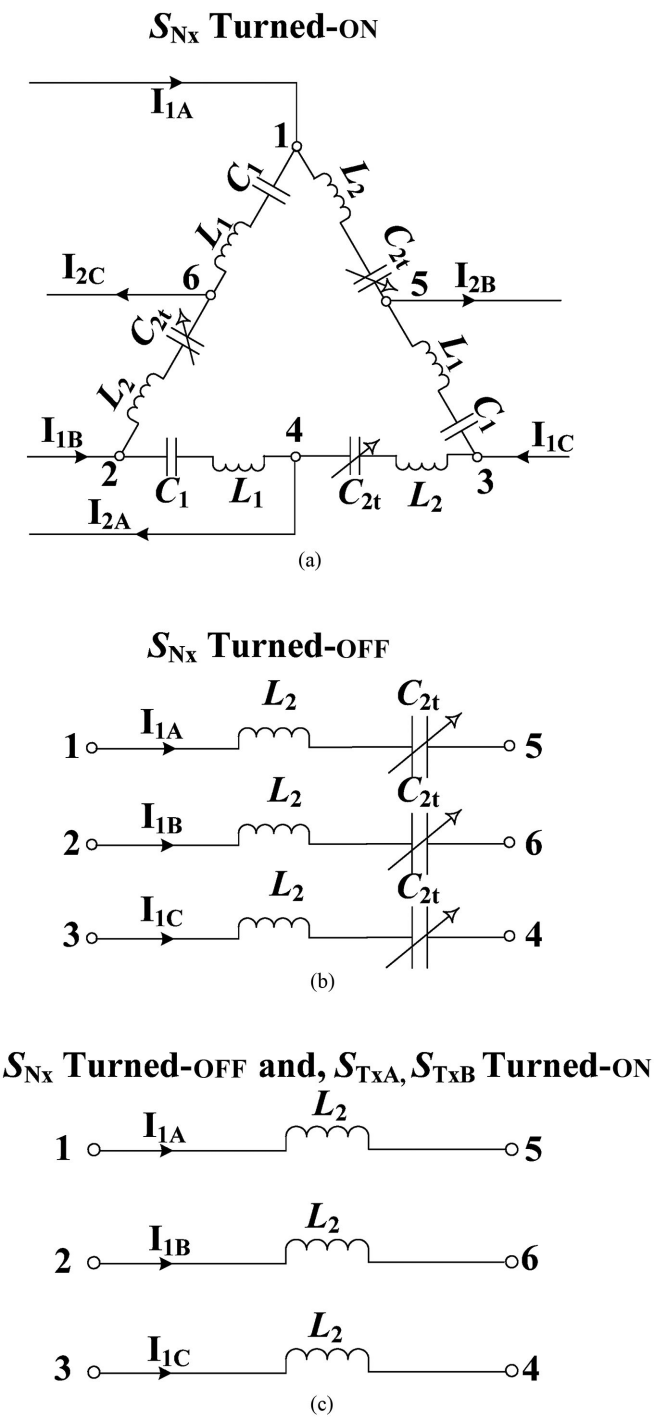

Fig. 2. (a) Three-phase TRIN. (b) Three-phase TSRN. (c) Three-phase series inductors.

III. Proposed 3p-DAB Converter With 3p-RTRN

The schematic diagram of the proposed converter is shown in Fig. 3. The proposed converter comprises two three-phase half-bridges interfaced by three Y–Y-connected high-frequency isolation transformers and the 3p-RTRN. The complimentary switch pairs S_{j1}/S_{j2} and Q_{j1}/Q_{j2} (where j = A, B, and C) in the primary and secondary bridges are operated with a fixed duty cycle of 0.5 and variable switching frequency $f_{\mathrm{s,\,min}} \leq f_{\mathrm{s}} \leq f_{\mathrm{s,\,max}}$. Moreover, the complimentary switch pairs in the adjacent phase legs of primary and secondary bridges are phase-shifted by 120° (e.g., S_{A1}/S_{A2} and S_{B1}/S_{B2} have a phase shift of 120°). In addition, there exists an external phase shift θ between the complimentary switch pairs of the corresponding phase legs in the primary and secondary bridges (e.g., S_{A1}/S_{A2} and Q_{A1}/Q_{A2} are phase-shifted by θ). In this way, the primary bridge generates three two-level ($+V_{\mathrm{in}}$/2, $-V_{\mathrm{in}}$/2) high-frequency square-wave ac voltages $v'_{1j}(t)$ (where j = A, B, and C) having a fixed 120° phase shift between the adjacent phase voltages. Similarly, a second set of three-phase two-level ($+V_{\mathrm{o}}$/2, $-V_{\mathrm{o}}$/2) square-wave ac voltages $v_{2j}(t)$ (where j = A, B, and C) is generated by the secondary bridge. Moreover, $v'_{1j}(t)$ and $v_{2j}(t)$ are phase-shifted by θ with θ defined as positive when $v'_{1j}(t)$ leads $v_{2j}(t)$.

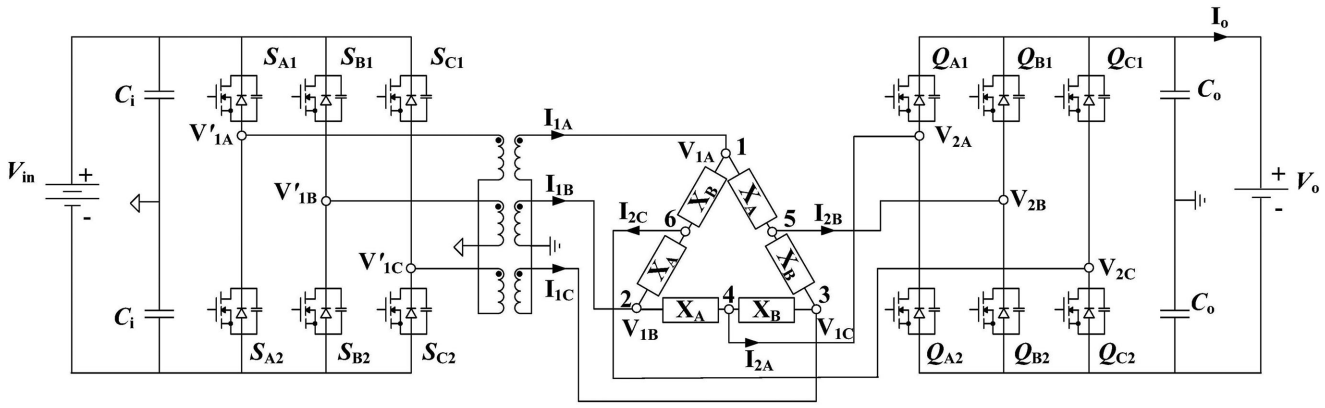

Fig. 3. Proposed 3p-DAB converter with the 3p-RTRN.

For ease of analysis, the primary-side voltages $v'_{1j}(t)$ and currents $i'_{1j}(t)$ are reflected to the secondary side (i.e., $v_{1j}(t)$ and $i_{1j}(t)$) to obtain an equivalent circuit without transformers. The three-phase square-wave ac voltages $v_{1j}(t)$ and $v_{2j}(t)$ are subsequently represented by their Fourier series expansions as

$$v_{1j}(t) = \frac{2V_{\rm in}}{n\pi} \sum_{k=1,3,\ldots}^{\infty} \frac{1}{k} \sin\left(k\omega_s t + f(j)\frac{2\pi}{3}\right) \tag{1}$$

$$v_{2j}(t) = \frac{2V_{\rm o}}{\pi} \sum_{k=1,3,\ldots}^{\infty} \frac{1}{k} \sin\left(k\omega_s t - k\theta + f(j)\frac{2\pi}{3}\right) \tag{2}$$

where $f(j) = (0, +1, -1)$ when $j = (\mathrm{A}, \mathrm{B}, \mathrm{C})$, $\omega_s = 2\pi f_s$, and $n = \frac{N_p}{N_s}$ is the transformer's turns ratio.

It is assumed that higher order voltage and current harmonics are attenuated by the resonant network. By applying fundamental component analysis, the fundamental components of $v_{1j}(t)$ and $v_{2j}(t)$ can be represented in phasor form as $\mathbf{V}_{1j}$ and $\mathbf{V}_{2j}$, respectively. Hence, $\mathbf{V}_{1j}$ and $\mathbf{V}_{2j}$ can be written as

$$\begin{aligned}\mathbf{V}_{1j} &= V_{1j}\angle\left(0 + f(j)\frac{2\pi}{3}\right) \\ &= \frac{\sqrt{2}V_{\rm in}}{n\pi}\angle\left(0 + f(j)\frac{2\pi}{3}\right) \end{aligned} \tag{3}$$

$$\begin{aligned}\mathbf{V}_{2j} &= V_{2j}\angle -\left(\theta + f(j)\frac{2\pi}{3}\right) \\ &= \frac{\sqrt{2}V_{\rm o}}{\pi}\angle -\left(\theta + f(j)\frac{2\pi}{3}\right). \end{aligned} \tag{4}$$

Depending upon the state of switches $S_{\mathrm{N}x}$ in the 3p-RTRN, the proposed converter can transform between a tunable 3p-DABRIC and a tunable 3p-DABSRC. The detailed discussions on the modeling and analysis for each of the two network configurations are presented in the following sections.

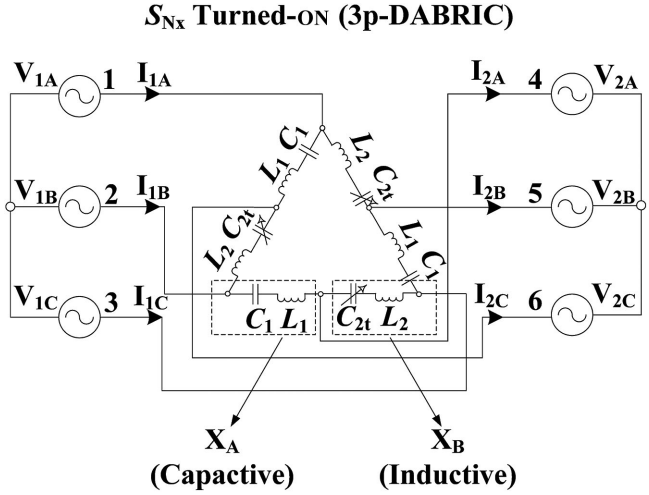

Fig. 4. Equivalent circuit of the proposed converter with the 3p-TRIN.

IV. Modeling and Analysis of Tunable 3p-DABRIC

A. Power Flow Analysis

Considering the case when the switches $S_{\mathrm{N}x}$ in branch $\mathbf{X_A}$ are turned ON, the impedances $\mathbf{X_A}$ enter into the resonant network and the converter transforms to a tunable 3p-DABRIC that can be represented by the equivalent circuit, as shown in Fig. 4. The magnitudes of the impedances $\mathbf{X_A}$ and $\mathbf{X_B}$ are given by (5), whereas the angular series resonance frequencies $\omega_{\rm a}$ and $\omega_{\rm b}$ of $\mathbf{X_A}$ and $\mathbf{X_B}$ are given by (6)

$$\begin{aligned}|\mathbf{X_A}| &= X_{\rm A} = \left|\omega_{\rm s}L_1 - \frac{1}{\omega_{\rm s}C_1}\right| \\ |\mathbf{X_B}| &= X_{\rm B} = \left|\omega_{\rm s}L_2 - \frac{1}{\omega_{\rm s}C_{2\rm t}}\right| \end{aligned} \tag{5}$$

$$\begin{aligned}\omega_{\rm a} &= \frac{1}{\sqrt{L_1C_1}} \\ \omega_{\rm b} &= \frac{1}{\sqrt{L_2C_{2\rm t}}}. \end{aligned} \tag{6}$$

Recall that $\mathbf{X_A}$ is constrained to operate below ω_a (i.e., $\omega_a > \omega_s$) to constitute an overall capacitive impedance to the network. On the contrary, $\mathbf{X_B}$ is constrained to operate above ω_b (i.e., $\omega_b < \omega_s$) to constitute an overall inductive impedance to the network. There exists a specific frequency at which the impedances $\mathbf{X_A}$ and $\mathbf{X_B}$ are equal in magnitude and opposite in phase such that they resonate with each other. The resonance frequency at which $\mathbf{X_A} = -\mathbf{X_B}$ can be found by solving $|\mathbf{X_A}| = |\mathbf{X_B}|$, and the resulting expression is given by

$$\omega_r = \sqrt{\frac{(C_1 + C_{2t})}{C_1 C_{2t}(L_1 + L_2)}}. \tag{7}$$

When operated at ω_r (i.e., $\omega_r = \omega_s$), the resonant network exhibits immittance characteristics, and the line currents $\mathbf{I}_{1j}$ at the input ports become linearly dependent on the phase voltages $\mathbf{V}_{2j}$ at the output ports. Similarly, the line currents $\mathbf{I}_{2j}$ at the output ports become linearly dependent on the phase voltages $\mathbf{V}_{1j}$ at the input ports. In other words, source transformation occurs at $\omega_r = \omega_s$ and the voltage sources $\mathbf{V}_{1j}$ at the input ports are transformed into current sources $\mathbf{I}_{2j}$ at the output ports. Under immittance conditions $|\mathbf{X_A}| = |\mathbf{X_B}| = X$, the expressions for the line currents $\mathbf{I}_{1j}$ and $\mathbf{I}_{2j}$ at input and output ports can be found by applying nodal analysis at different nodes of the resonant network, and the results are given by (8) and (9). The detailed derivation of these expressions and a detailed analysis of the effects of component tolerances on the immittance network's characteristics has been presented previously in [21] and will not be repeated here due to space constraint

$$\begin{aligned}\mathbf{I}_{1j} &= I_{1j}\angle -\left(\theta + f(j)\frac{2\pi}{3}\right) \\ &= \frac{\sqrt{6}V_o}{\pi X}\angle -\left(\theta + f(j)\frac{2\pi}{3}\right) \end{aligned} \tag{8}$$

$$\begin{aligned}\mathbf{I}_{2j} &= I_{2j}\angle\left(0 + f(j)\frac{2\pi}{3}\right) \\ &= \frac{\sqrt{6}V_{in}}{n\pi X}\angle\left(0 + f(j)\frac{2\pi}{3}\right) \end{aligned} \tag{9}$$

$$\text{where} X = \left|\omega_r L_1 - \frac{1}{\omega_r C_1}\right| = \left|\omega_r L_2 - \frac{1}{\omega_r C_{2t}}\right|.$$

By inspecting (3), (4), (8), and (9), it can be seen that there exists a phase difference equal to the phase shift θ between $\mathbf{V}_{1j}$ and $\mathbf{I}_{1j}$ and between $\mathbf{V}_{2j}$ and $\mathbf{I}_{2j}$. By setting $\theta = 0$, an in-phase relationship (i.e., UPF operation) can be achieved between $\mathbf{V}_{1j}$ and $\mathbf{I}_{1j}$ and between $\mathbf{V}_{2j}$ and $\mathbf{I}_{2j}$ at all ports of the immittance network, as depicted in the phasor diagrams of Fig. 5.

Considering the converter as being lossless, the expression for the converter's output power P_o can be derived by finding the output power expression for a single phase (e.g., phase A) and multiplying the resulting expression by three, as given by

$$\begin{aligned}P_o &= 3 \times \Re[\mathbf{V_{1A}}\mathbf{I}^*_{\mathbf{1A}}] = 3 \times \Re[\mathbf{V_{2A}}\mathbf{I}^*_{\mathbf{2A}}] \\ &= \frac{3\sqrt{12}V_{in}V_o}{n\pi^2 X}\cos(\theta). \end{aligned} \tag{10}$$

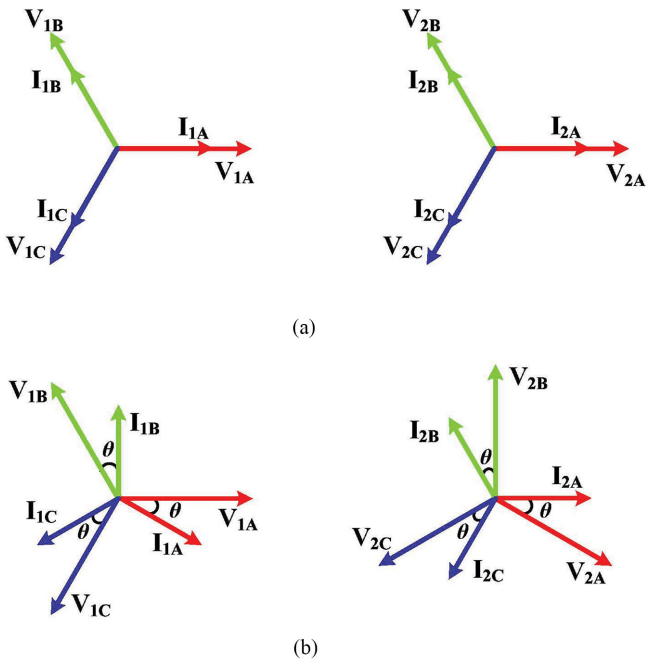

Fig. 5. (a) Phasor relationship between $\mathbf{V}_{1j}$ and $\mathbf{I}_{1j}$ and between $\mathbf{V}_{2j}$ and $\mathbf{I}_{2j}$ for $\theta = 0$. (b) Phasor relationship between $\mathbf{V}_{1j}$ and $\mathbf{I}_{1j}$ and between $\mathbf{V}_{2j}$ and $\mathbf{I}_{2j}$ for $\theta \neq 0$.

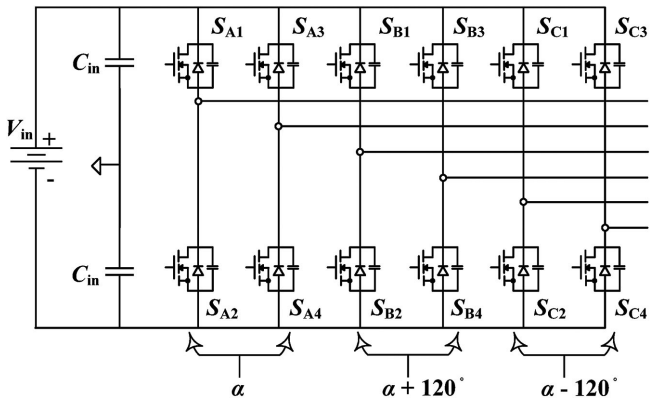

Fig. 6. Three-phase full-bridge structure proposed in [21] and [26].

Inspection of (10) reveals that one of the control variables available for modulating output power of 3p-DABRIC is the phase shift θ. However, since θ is constrained to be zero for achieving UPF operation, it is necessary to utilize other control variables for controlling the output power. The authors have previously proposed an application of three-phase full-bridge in 3p-DABRIC, with which the internal phase shift α between the two legs of the same full-bridge is used as a control variable for modulating output power (cf. Fig. 6) [21], [26]. By utilizing an internal phase shift between S_{j1}/S_{j2} and S_{j3}/S_{j4} in the range $0 \leq \alpha \leq 180°$, three-phase three-level $(+V_{in}, 0, -V_{in})$ pulsewidth modulated symmetrical ac voltages $\mathbf{V}_{1j}$ with variable duty ratio can be generated by this bridge structure. In this way, the converter's output power can be controlled by modulating the pulsewidth of the input port voltages $\mathbf{V}_{1j}$ as a function of the

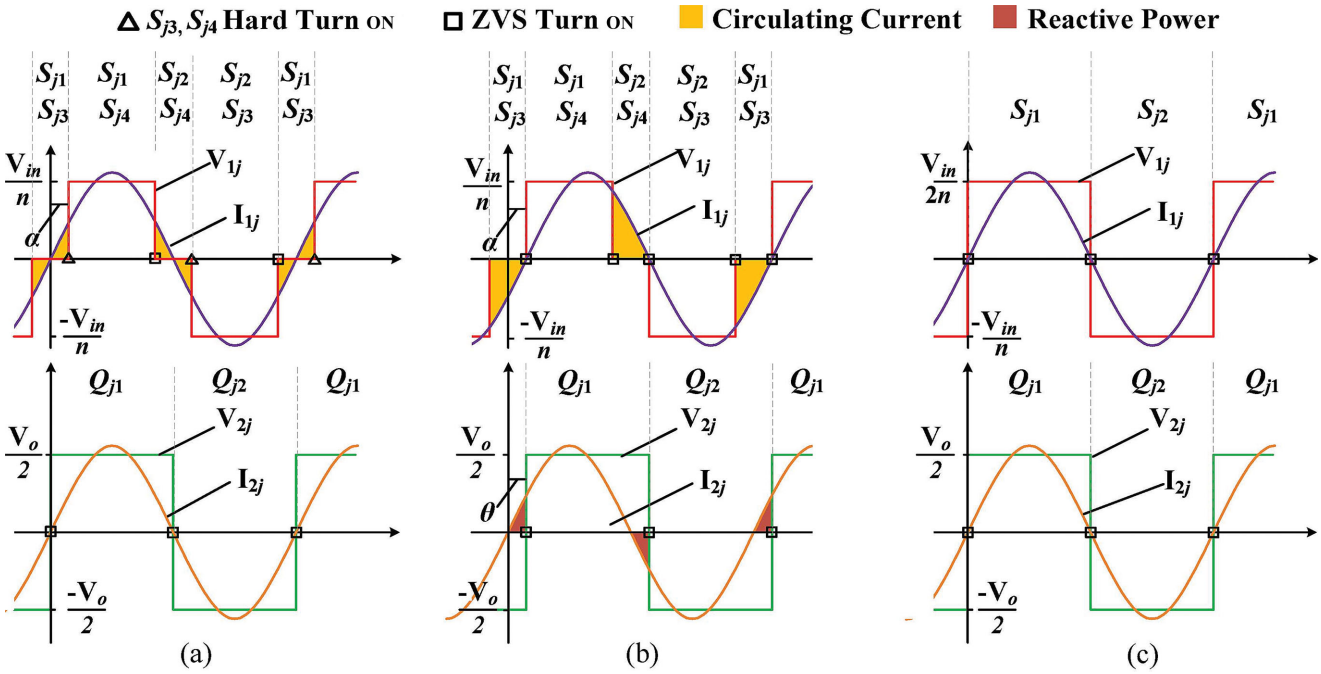

Fig. 7. (a) Port currents and port voltages for UPF operation. (b) Port currents and port voltages for full-range ZVS operation. (c) Port currents and port voltages for the proposed DFM modulation.

internal phase shift α while maintaining a UPF at all ports of the immittance network. Under this control scheme, $\mathbf{V}_{1j}$ and $\mathbf{I}_{1j}$, and similarly for $\mathbf{V}_{2j}$ and $\mathbf{I}_{2j}$, are constantly in-phase with each other [cf. Fig. 7(a)], which leads to minimum rms port currents and conduction loss. However, the major drawback of this control method is that the complimentary switches S_{j3} and S_{j4} in the lagging leg of each phase are hard switched [cf. Fig. 7(a)], leading to increased switching loss.

In order to mitigate switching loss and achieve ZVS commutation for all switches, a two-DoF control scheme has been proposed previously that utilizes both α and θ simultaneously (i.e., $\alpha = \theta$) for controlling output power. By introducing θ between $\mathbf{V}_{1j}$ and $\mathbf{V}_{2j}$, $\mathbf{V}_{1j}$ leads $\mathbf{I}_{1j}$ at the input ports by θ and $\mathbf{V}_{2j}$ lags $\mathbf{I}_{2j}$ at the output ports by θ leading to ZVS turn-ON of all the switches [cf. Figs. 5(b) and 7(b)]. However, the major drawback of this control method is that high circulating current and reactive power prevail under light-load conditions [cf. highlighted by the shaded areas in Fig. 7(b)], which leads to increased conduction loss. It can be safely inferred that the existing approaches cannot concurrently minimize conduction and switching losses in the 3p-DABRIC; therefore, it is necessary to devise a new approach that can overcome this restriction for achieving a wide-range high-efficiency performance.

B. Proposed Modulation Scheme for a Tunable 3p-DABRIC

By inspection of (10), it can be observed that the switching frequency $\omega_{\rm s}$ can be used to control the output power of the 3p-DABRIC. However, since $\omega_{\rm r}$ must be tuned to match with $\omega_{\rm s}$ to meet the immittance conditions (i.e., $|\mathbf{X_A}| = |\mathbf{X_B}| = X$), it is necessary to modulate $\omega_{\rm r}$ in synchronism with $\omega_{\rm s}$. For modulating $\omega_{\rm r}$, SCCs are used to realize electronically tunable capacitors C_{2t} in the immittance network with tunable $\omega_{\rm r}$. Thus, by modulating $\omega_{\rm s}$ and $\omega_{\rm r}$ concurrently (i.e., DFM), X can be varied and the 3p-DABRIC's output power can be controlled according to (10). The port voltages $\mathbf{V}_{1j}$ and $\mathbf{V}_{2j}$ and port currents $\mathbf{I}_{1j}$ and $\mathbf{I}_{2j}$ under the proposed DFM modulation are shown in Fig. 7(c). It can be seen from Fig. 7(c) that the proposed modulation method enables a control of output power while achieving UPF operation and zero circulating current. Moreover, as the zero crossings of i_{1x} and i_{2x} are always aligned with the rising edges of v_{1x} and v_{2x}, all switches inherently undergo ZVS commutation. Due to the elimination of circulating current, UPF operation, and ZVS commutation of all switches, the proposed DFM modulation scheme is anticipated to yield a wide-range high-efficiency performance, as will be validated by experimental results in Section VI.

To derive the expression for the output power under DFM modulation and define the controllable range of P_o, X, and $\omega_{\rm s}$, it is necessary to describe the operating principle of the SCC. Recall that the switches $S_{\rm TxA}$ and $S_{\rm TxB}$ and capacitor C_2 in branch $\mathbf{X_B}$ constitute the SCC, which acts as an electronically controllable capacitor $C_{2\rm t}$, as shown in Fig. 8(a). The operating principle of the SCC can be explained by referring to the timing diagram for SCC, as shown in Fig. 8(b), where $i_{C_{2\rm t}}$ is the sinusoidal current flowing through $C_{2\rm t}$, $v_{C_{2\rm t}}$ is the voltage across C_2, ψ is the control angle of $S_{\rm TxA}$ and $S_{\rm TxB}$, and T is the period of $i_{C_{2\rm t}}$. The gating signals for $S_{\rm TxA}$ are applied for a duration of $\frac{\psi T}{2\pi}$ at the negative-to-positive zero-crossing instant of $i_{C_{2\rm t}}$, while the gating signals with the same pulsewidth are applied to $S_{\rm TxB}$ at the positive to negative zero-crossing instant of $i_{C_{2\rm t}}$. At $\omega t = \pi - \psi$, the voltage $v_{C_{2\rm t}}$ across C_2 is zero and $i_{C_{2\rm t}}$

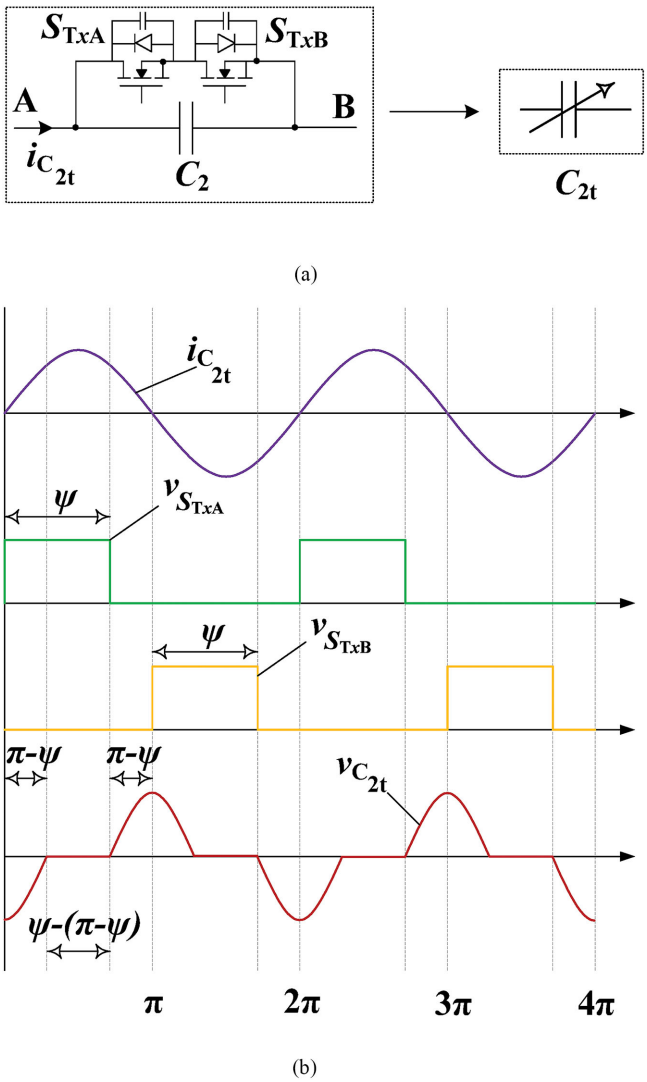

Fig. 8. (a) Schematic diagram of the SCC. (b) Timing diagram of the SCC.

flows from A to B through S_{TxA} and the body diode of S_{TxB}. At $\omega t = \psi$, S_{TxA} is turned OFF and $i_{C_{2t}}$ flows from A to B through C_2, thus charging it for a duration of $\frac{(\pi-\psi)T}{2\pi}$. At the positive-to-negative transition of $i_{C_{2t}}$ (i.e., $\omega t = \pi$), S_{TxB} is turned ON, $i_{C_{2t}}(t)$ starts flowing in the opposite direction from B to A through C_2, thus discharging it to zero. During the next zero-voltage state of v_{C2t}, $i_{C_{2t}}$ flows from B to A through S_{TxB} and the body diode of S_{TxA} until S_{TxB} is turned OFF at $\omega t = (\pi + \psi)$ followed by the charging of C_2 by the negative flowing $i_{C_{2t}}$.

It can be inferred from Fig. 8(b) that the control angle ψ provides a means to control the charging/discharging time (i.e., $\frac{(\pi-\psi)T}{2\pi}$) of C_2 and consequently determines the magnitude of the fundamental component of v_{C2t} for a given $i_{C_{2t}}$[29]. By considering the fundamental component of $v_{C_{2t}}$, an expression for the effective capacitance C_{2t} can be derived as a function of control angle ψ, as given by (11). The derivation of this expression can be found in [30]. Moreover, it should also be noted that S_{TxA} and S_{TxB} turn ON and OFF at zero voltage and

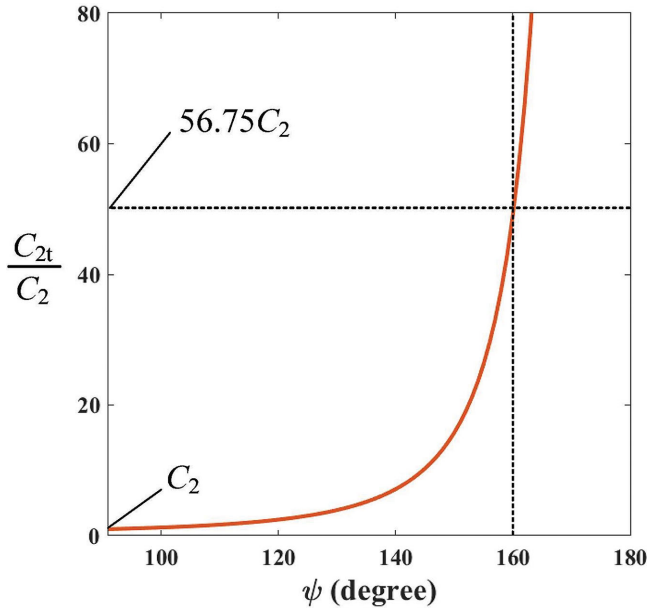

Fig. 9. Effective SCC capacitance C_{2t} versus control angle ψ.

thus incur negligible commutation loss

$$C_{2t}(\psi) = \frac{\pi C_2}{2\pi - 2\psi + \sin 2\psi}. \tag{11}$$

C. Design Considerations for Tunable 3p-DABRIC Under DFM Modulation

Based on (11), C_{2t} can be varied theoretically in the range $C_2 \leq C_{2t} \leq \infty$ corresponding to $90^\circ \leq \psi \leq 180^\circ$. A plot of C_{2t}/C_2 versus ψ is depicted in Fig. 9, where it can be seen that C_{2t} increases nonlinearly with increasing ψ and tends to ∞ as $\psi \longrightarrow 180^\circ$. To have a reasonable range of C_{2t} with good controllability, the values of C_{2t} and ψ should be restricted, for example, $C_2 \leq C_{2t} \leq \kappa C_2$ and $90^\circ \leq \psi \leq 160^\circ$, respectively, with $\kappa = 56.75$ (cf. Fig. 9). It should be noted that the value of κ is dependent on the maximum value of ψ and can be obtained from (11). Furthermore, by substituting (11) into (7), an expression for ω_r can be obtained as a function of control angle ψ, as given by

$$\omega_r(\psi) = \sqrt{\frac{2\pi C_1 + \pi C_2 - 2C_1\psi + C1\sin(2\psi)}{\pi C_1 C_2 (L_1 + L_2)}}. \tag{12}$$

By inspection of (12), it can be observed that ω_r can be tuned to match with ω_s by means of varying ψ in the range of $160^\circ \geq \psi \geq 90^\circ$ to give $\omega_{r,min} \leq \omega_r \leq \omega_{r,max}$. An expression for $\omega_{r,min}$ and $\omega_{r,max}$ can be obtained by substituting the extreme values of ψ (i.e., $\psi = 160^\circ$ and $\psi = 90^\circ$, respectively) into (12). The resulting expressions for $\omega_{r,min}$ and $\omega_{r,max}$ are given by

$$\omega_{r,min} = \sqrt{\frac{(C_1 + \kappa C_2)}{C_1 \kappa C_2 (L_1 + L_2)}}$$

$$\omega_{r,max} = \sqrt{\frac{(C_1 + C_2)}{C_1 C_2 (L_1 + L_2)}} = \sigma \omega_{r,min}. \tag{13}$$

By setting $\theta = 0^\circ$ in (10), an expression for the output power as a function of ψ can be obtained as

$$P_o(\psi) = \frac{3\sqrt{12}V_{\rm in}V_{\rm o}}{n\pi^2 X(\psi)} \tag{14}$$

where $X(\psi) = \left|\omega_{\rm r}L_1 - \frac{1}{\omega_{\rm r}C_1}\right| = \left|\omega_{\rm r}L_2 - \frac{1}{\omega_{\rm r}C_{2\rm t}}\right|$.

By dividing (14) with $V_{\rm o}$, the expression for the output current of 3p-DABRIC can be obtained as

$$I_o(\psi) = \frac{3\sqrt{12}V_{\rm in}}{n\pi^2 X(\psi)}. \tag{15}$$

The expressions for $P_{\rm o,min}$ and $P_{\rm o,max}$ corresponding to $\omega_{\rm r,min}$ and $\omega_{\rm r,max}$, respectively, can be obtained by substituting (13) into (14). The results are given by (16) and (17), as follows:

$$P_{\rm o,min} = \frac{3\sqrt{12}V_{\rm in}V_{\rm o}}{n\pi^2 X_{\max}} \tag{16}$$

where

$$X_{\max} = \left|\omega_{\rm r,min}L_1 - \frac{1}{\omega_{\rm r,min}C_1}\right| = \left|\omega_{\rm r,min}L_2 - \frac{1}{\omega_{\rm r,min}\kappa C_2}\right|.$$

$$P_{\rm o,max} = \frac{3\sqrt{12}V_{\rm in}V_{\rm o}}{n\pi^2 X_{\min}} = \epsilon P_{\rm o,min} \tag{17}$$

where

$$X_{\min} = \left|\omega_{\rm r,max}L_1 - \frac{1}{\omega_{\rm r,max}C_1}\right| = \left|\omega_{\rm r,max}L_2 - \frac{1}{\omega_{\rm r,max}C_2}\right|.$$

By inspection of (16) and (17), it can be observed that there is a certain range of output power $P_{\rm o}$ (i.e., medium-to-high output power levels) that can be attained by the proposed DFM modulation. Moreover, $P_{\rm o}$ is directly proportional to $\omega_{\rm r}$, and to reduce output power, $\omega_{\rm r}$ needs to be reduced by increasing ψ. Nevertheless, below $P_{\rm o,min}$, the output power cannot be reduced further by DFM modulation as ψ reaches its maximum value. Therefore, below $P_{\rm o,min}$ corresponding to $\omega_{\rm r,min}$, it is proposed to reconfigure the converter to a tunable 3p-DABSRC for operation in low-power range. The detailed analysis and the proposed modulation scheme for the tunable 3p-DABSRC is presented in the next section. As the desired ranges of P_o and $\omega_{\rm r}$ [cf. (12)–(17)] depend on the selection of passive component values, the key design equations for L_1, L_2, C_1, and C_2 as a function of the multiplier terms (ϵ, σ, and κ) can be obtained by simultaneously solving (16) and (17). The results are given by

$$L_1 = \frac{X_{\min}\sigma(\epsilon - \sigma)}{\omega_{\rm r,max}(\sigma^2 - 1)} \tag{18}$$

$$L_2 = \frac{X_{\min}\sigma(\kappa\epsilon - \sigma)}{\omega_{\rm r,max}(\kappa - \sigma^2)} \tag{19}$$

$$C_1 = \frac{\sigma^2 - 1}{X_{\min}\omega_{\rm r,max}(\sigma\epsilon - 1)} \tag{20}$$

$$C_2 = \frac{\kappa - \sigma^2}{\kappa X_{\min}\omega_{\rm r,max}(\kappa\sigma\epsilon - 1)}. \tag{21}$$

By inspection of (18)–(21), it can be observed that while selecting the values of the multiplier terms (i.e., ϵ, σ, and κ) for a given $P_{\rm o,max}$ and $\omega_{\rm r,max}$, the constraints $\epsilon > \sigma$, $\sigma > 1$, $\kappa\epsilon > 1/\sigma$, and $\kappa > \sigma^2$ must be adhered to. Furthermore, by substituting (18)–(21) into (6), the new expressions for $\omega_{\rm a}$ and $\omega_{\rm b}$ can be obtained in terms of ψ, σ, and κ as given by

$$\omega_{\rm a} = \sqrt{\frac{\omega_{\rm r,max}^2(\sigma\epsilon - 1)}{\sigma(\epsilon - \sigma)}}$$

$$\omega_{\rm b}(\psi) = \sqrt{\frac{\kappa\omega_{\rm r,max}^2(\sigma\epsilon - 1)}{{\rm A}\sigma(\epsilon\kappa - \sigma)}} \tag{22}$$

where ${\rm A} = \dfrac{\pi}{2\pi - 2\psi + 2\sin(2\psi)}$.

By dividing (22) with (12), the ratios $\dfrac{\omega_{\rm a}}{\omega_{\rm r}(\psi)}$ and $\dfrac{\omega_{\rm b}(\psi)}{\omega_{\rm r}(\psi)}$ can be obtained as given by (23). These ratios are important design parameters as they determine the voltage stress across the passive components in the immittance network and the shape of the network's current waveforms. Moreover, these ratios describe how far the branch impedances $\mathbf{X_A}$ and $\mathbf{X_B}$ are operating from their series resonance frequencies $\omega_{\rm a}$ and $\omega_{\rm b}$. A value closer to unity for these ratios implies stronger resonance, higher voltage stress, and more sinusoidal current waveforms, and *vice versa*

$$\frac{\omega_{\rm a}}{\omega_{\rm r}(\psi)} = \sqrt{\frac{{\rm A}\sigma^2\omega_{\rm r,max}^2(\sigma\varepsilon - 1)(\kappa - 1)}{\sigma\omega_{\rm r,max}^2(\sigma - \varepsilon)\left(\kappa + {\rm A}\sigma^2 - \sigma^2\kappa - {\rm A}\kappa\right)}}$$

$$\frac{\omega_{\rm b}(\psi)}{\omega_{\rm r}(\psi)} = \sqrt{\frac{{\rm A}\sigma^2\kappa\omega_{\rm r,max}^2(\sigma\epsilon - 1)(\kappa - 1)}{{\rm A}\sigma\omega_{\rm r,max}^2(\sigma - \kappa\epsilon)\left(\kappa + {\rm A}\sigma^2 - \sigma^2\kappa - {\rm A}\kappa\right)}}. \tag{23}$$

By utilizing (18)–(23), the range of controllable output power, switching frequency, and control angle for the DFM-modulated 3p-DABRIC can be selected appropriately to have adequate voltage stress across the SCC, good sinusoidal current waveforms, and a narrow switching frequency range.

V. Modeling and Analysis of Tunable 3p-DABSRC

Recall that the proposed DFM modulation scheme should not be used for modulating output power below $P_{\rm o,min}$. Although the DFM modulation scheme completely eliminates circulating current and achieves full-range ZVS operation, its implementation is constrained by the minimum allowable switching frequency. Therefore, below $P_{\rm o,min}$, which is associated with $\omega_{\rm r,min}$, it is proposed to reconfigure the converter to a tunable 3p-DABSRC and use impedance modulation for modulating output power while keeping the switching frequency constant. In addition, the phase shift θ is kept constant as determined by the input-to-output voltage ratio to achieve full-range ZVS operation and maintain minimum-tank-current operation simultaneously for minimizing switching and conduction losses, respectively [29]. As a result, the proposed reconfiguration will enable high-efficiency performance for light-load operation as well.

A. Power Flow Analysis

For reconfiguration to a tunable 3p-DABSRC, the switches $S_{{\rm N}x}$ in branch $\mathbf{X_A}$ are turned OFF (cf. Fig. 10). This action

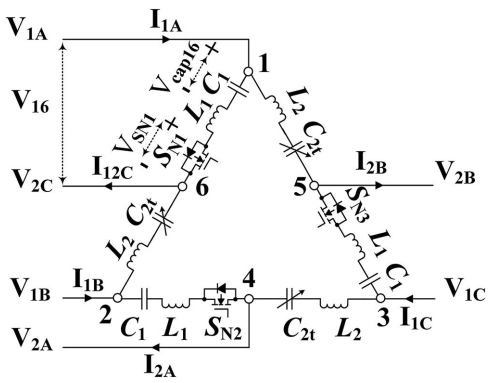

Fig. 10. Voltage distribution across branch $\mathbf{X_A}$.

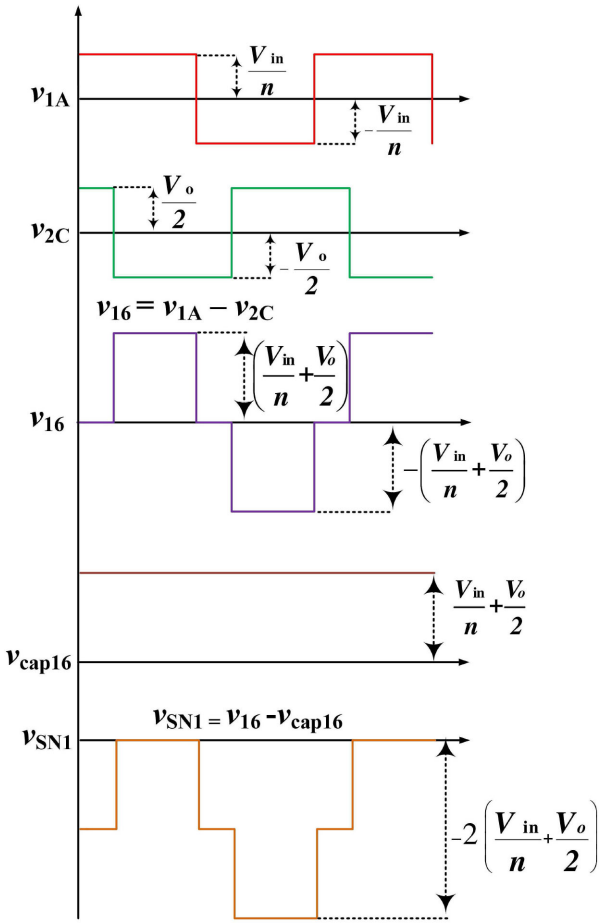

Fig. 11. Voltage waveforms across capacitor C_1 and switch S_{N1} for 3p-DABSRC.

isolates the impedances $\mathbf{X_A}$ from the resonant network and only impedances $\mathbf{X_B}$ are active. Referring to Fig. 10, when S_{N1} (the same argument applies to S_{N2} and S_{N3}) is turned OFF, the capacitor C_1 in $\mathbf{X_A}$ is charged to the maximum voltage $(\frac{V_{\mathrm{in}}}{n}+\frac{V_o}{2})$ by the voltage difference $v_{1\mathrm{A}}-v_{2\mathrm{C}}$ (cf. Fig. 11). As a result, the voltage seen by S_{N1}, i.e., $v_{1\,\mathrm{A}}-v_{2\,\mathrm{C}}-v_{\mathrm{cap16}}$ will vary between 0 and $-2(\frac{V_{\mathrm{in}}}{n}+\frac{V_o}{2})$, which will always keep the body diode of S_{N1} in a reverse biased state. Therefore, $\mathbf{X_A}$ can be fully isolated by using only a two-quadrant switch. Furthermore, to operate

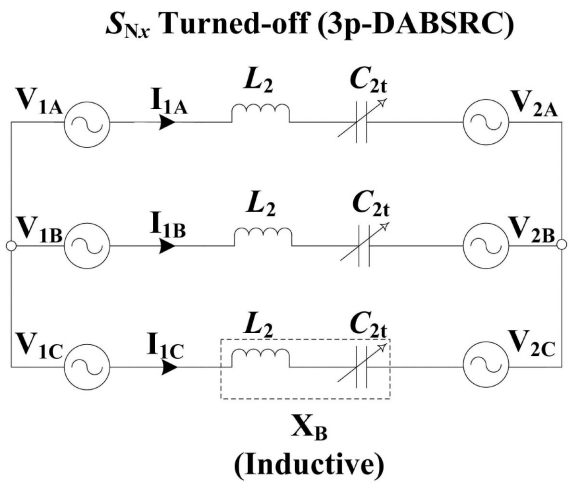

Fig. 12. Equivalent circuit of the proposed converter with the 3p-TSRN.

the converter as a tunable 3p-DABSRC, phase transposition must be applied at the output ports of the network, i.e., $\mathbf{V}_{2j}$ are to be phase-shifted by 120° so that the voltages at the input and output ports of the network correspond with each other. The effects of these two operations (i.e., $S_{\mathrm{N}x}$ are turned OFF and phase transposition is applied at the output ports) are to transform the converter to a tunable 3p-DABSRC, as depicted by the equivalent circuit shown in Fig. 12. Considering the case where power is transferred from $\mathbf{V}_{1j}$ to $\mathbf{V}_{2j}$ (i.e., $\mathbf{V}_{1j}$ leads $\mathbf{V}_{2j}$), the port currents $\mathbf{I}_{1j}$ can be obtained by applying Ohm's law, as given by

$$\mathbf{I}_{1j} = \frac{\mathbf{V}_{1j}-\mathbf{V}_{2j}}{\mathbf{X}_{\mathrm{B}}} = I_{1j}\angle -\left(\phi + f(j)\frac{2\pi}{3}\right)$$
$$I_{1j} = \frac{\sqrt{2}\,V_{\mathrm{in}}\sqrt{1-2\,G\cos(\theta)+G^2}}{n\pi X_{\mathrm{B}}}$$
$$\phi = \left(\tan^{-1}\left(\frac{1-G\cos(\theta)}{G\sin(\theta)}\right)\right) \tag{24}$$

where $G = nV_{\mathrm{o}}/V_{\mathrm{in}}$.

By using (3) and (24), an expression for the output power of 3p-DABSRC can be obtained as

$$P_{\mathrm{o}} = 3\times\Re[\mathbf{V}_{1\,\mathbf{A}}\mathbf{I}^*_{1\,\mathbf{A}}]$$
$$= \frac{6V_{\mathrm{in}}V_{\mathrm{o}}}{n\pi^2 X_{\mathrm{B}}}\sin(\theta). \tag{25}$$

By dividing (25) with V_{o}, the expression for the output current of 3p-DABSRC can be obtained as

$$I_{\mathrm{o}} = \frac{6V_{\mathrm{in}}}{n\pi^2 X_{\mathrm{B}}}\sin(\theta). \tag{26}$$

By inspection of (24), it can be observed that unlike 3p-DABRIC, the phase angle ϕ of $\mathbf{I}_{1j}$ of the 3p-DABSRC is dependent on the voltage ratio G. For ZVS operation of the 3p-DABSRC, the value of ϕ should be in the range $0 \le \phi \le \theta$ so that $\mathbf{I}_{1j}$ lags $\mathbf{V}_{1j}$ and leads $\mathbf{V}_{2j}$. This implies that the instantaneous current should be negative at the turn-ON instants of the primary-side switches S_{j1} (and positive for S_{j2}) and

positive at the turn-ON instants of the secondary-side switches Q_{j1} (and negative for Q_{j2}) (cf. Fig. 3) so that the switches' parasitic capacitances are discharged and their body diodes conduct before the gate signals are applied. Based on (24), when G is unity, the value of ϕ will be $\theta/2$, and the 3p-DABSRC will achieve ZVS operation independent of output power. However, deviation of G from unity causes ϕ to violate the constraint $0 \leq \phi \leq \theta$ resulting in hard switching and increased circulating current. Therefore, it is proposed to calculate θ based on the value of G such that ϕ resides in the range $0 \leq \phi \leq \theta$ and modulate output power by varying X_{B} [cf. (25)].

B. Criteria for ZVS and Minimum-Tank-Current Operation

Recall that for ZVS operation of all switches, ϕ should reside between 0 and θ, i.e., $0 \leq \phi \leq \theta$. Therefore, by evaluating $\phi \geq 0$ and $\phi \leq \theta$, the ZVS conditions for the primary- and secondary-side switches can be derived in terms of G and θ. The results are given by

$$\theta \geq \cos^{-1}(G) \quad \text{for} \quad \mathrm{G} < 1 \tag{27}$$

$$\theta \geq \cos^{-1}\left(\frac{1}{G}\right) \quad \text{for} \quad \mathrm{G} > 1. \tag{28}$$

Thus, θ can be selected as a function of G according to (27) and (28) to ensure ZVS operation of the 3p-DABSRC.

To determine the criteria for minimum-tank-current operation of the 3p-DABSRC, the port currents I_{1j} given by (24) are divided by the output current given by (26) to obtain a load independent and normalized expression for port current that is independent of X_{B}. The resulting expression is given by

$$I_{\mathrm{N}1j} = \frac{I_{1j}}{I_{\mathrm{o}}} = \frac{\sqrt{2}\,\pi\sqrt{1 - 2\,G\cos(\theta) + G^2}}{6\sin(\theta)}. \tag{29}$$

By inspection of (29), it can be seen that the normalized port currents $I_{\mathrm{N}1j}$ are function of G and θ only. To achieve minimum-tank-current operation, the minimum value of $I_{\mathrm{N}1j}$ is found by taking its first derivative (with respect to θ) and setting it to zero [29]. The results are given by

$$\frac{\mathrm{d}}{\mathrm{d}\theta}\left(I_{\mathrm{N}1j}\right) = 0 \Rightarrow \theta = \begin{cases} \cos^{-1}(G) & \forall G < 1 \\ \cos^{-1}\left(\dfrac{1}{G}\right) & \forall G > 1 \end{cases} \tag{30}$$

The conditions given by (30) (i.e., $\theta = \cos^{-1}(G)$ for $G < 1$ and $\theta = \cos^{-1}(1/G)$ for $G > 1$) form the criteria for minimum-tank-current operation of the 3p-DABSRC. To determine the phasor relationship between $\mathbf{V}_{1j}$, $\mathbf{V}_{2j}$, and $\mathbf{I}_{1j}$ under minimum-tank-current operation, the values of θ, as determined by (30), are substituted into (24) to obtain ϕ for different values of G. The resulting expression is given by

$$\phi = \begin{cases} \theta & \forall G < 1 \text{ and } \theta = \cos^{-1}(G) \\ \dfrac{\theta}{2} & \forall G = 1 \text{ and } \theta = \theta_{\min} \\ 0 & \forall G > 1 \text{ and } \theta = \cos^{-1}\left(\dfrac{1}{G}\right) \end{cases} \tag{31}$$

According to (31), under minimum-tank-current operation, $\mathbf{I}_{1j}$ should be in phase with $\mathbf{V}_{2j}$ for $G < 1$ [cf. Fig. 13(a) and (d)], and in phase with $\mathbf{V}_{1j}$ for $G > 1$ [cf. Fig. 13(c) and (f)]. Thus, it can be concluded that by selecting θ corresponding to (30) for different values of G, full-range ZVS and minimum-tank-current operation can be achieved for the 3p-DABSRC to minimize switching and conduction losses simultaneously.

C. Impedance Modulation and Design Considerations for Tunable 3p-DABSRC

After determining θ for a given G, the output power of 3p-DABSRC can be controlled by modulating impedance X_{B} as a function of ψ. By substituting (30) into (25), the expression for the output power of the 3p-DABSRC can be obtained as

$$P_{\mathrm{o}}(\psi) = \begin{cases} = \dfrac{6V_{\mathrm{in}}V_{\mathrm{o}}}{n\pi^2 X_{\mathrm{B}}(\psi)}\sin(\cos^{-1}(G)) & \forall G < 1 \\ = \dfrac{6V_{\mathrm{in}}V_{\mathrm{o}}}{n\pi^2 X_{\mathrm{B}}(\psi)}\sin(\theta_{\min}) & \forall G = 1 \\ = \dfrac{6V_{\mathrm{in}}V_{\mathrm{o}}}{n\pi^2 X_{\mathrm{B}}(\psi)}\sin\left(\cos^{-1}\left(\dfrac{1}{G}\right)\right) & \forall G > 1 \end{cases} \tag{32}$$

Since the maximum output power for the 3p-DABSRC is equal to the minimum output power for the 3p-DABRIC, the minimum series impedance $X_{\mathrm{B}_{\mathrm{SRC(min)}}}$ can be obtained from (16) and (32). The result is given by (33). By using (16) and (33), the switching frequency for 3p-DABSRC can be obtained as given by (34)

$$X_{\mathrm{B}_{\mathrm{SRC(min)}}} = \frac{6\epsilon V_{\mathrm{o}}V_{\mathrm{in}}\sin(\theta_{\min})}{n\pi^2 P_{\mathrm{o,max}}} \tag{33}$$

$$\omega_{\mathrm{s}} = \frac{\sqrt{(C_2 X_{\mathrm{B}_{\mathrm{SRC(min)}}})^2 + 4L_2C_2} + C_2 X_{\mathrm{B}_{\mathrm{SRC(min)}}}}{2L_2C_2}. \tag{34}$$

Thus, for a tunable 3p-DABSRC, the converter is operated with a constant switching frequency, as given by (34), and the output power is varied by modulating impedance X_{B} as a function of ψ.

VI. Prototype Design and the Experimental Results

To validate the effectiveness of the proposed converter and benchmark its performance, a laboratory prototype shown in Fig. 14 has been designed and built with the specifications listed in Table I. A flowchart depicting the detailed design procedure is shown in Fig. 15. The prototype has been designed to operate as a tunable 3p-DABRIC from 40% to 100% of the rated output power with variable switching frequency such that the switching frequency varies from 35 kHz at 40% to 50 kHz at 100% of the rated output power. The variation of f_{s} and ψ versus P_{o} is plotted in Fig. 16(a) by using (14). It can be seen from Fig. 16(a) that P_{o} varies from 40% to 100% of the rated output power as f_{s} varies from 35 to 50 kHz and ψ varies from 160° to 90°. It is reminded that under the proposed DFM modulation for the 3p-DABRIC, f_{s} and ψ are varied synchronously to maintain the immittance condition (i.e., $\omega_{\mathrm{r}} = \omega_{\mathrm{s}}$). Below 40% of the rated output power (i.e., $P_{\mathrm{o}} \leq P_{\mathrm{o,max}}/\sigma$), the converter is reconfigured to a tunable

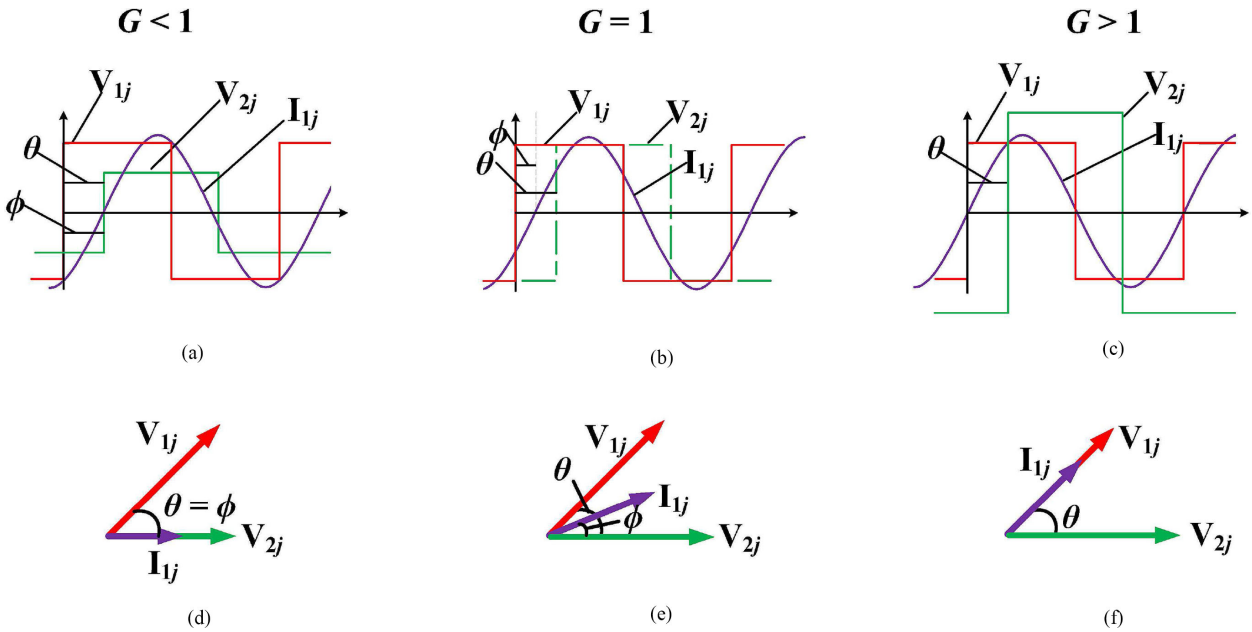

Fig. 13. Port currents and voltages of a tunable 3p-DABSRC using the impedance modulation scheme for different voltage ratios G. (a) $G < 1$. (b) $G = 1$. (c) $G > 1$. (d) Phasor relationship between $\mathbf{V}_{1j}$, $\mathbf{V}_{2j}$, and $\mathbf{I}_{1j}$ for $G < 1$. (e) Phasor relationship between $\mathbf{V}_{1j}$, $\mathbf{V}_{2j}$, and $\mathbf{I}_{1j}$ for $G = 1$. (f) Phasor relationship between $\mathbf{V}_{1j}$, $\mathbf{V}_{2j}$, and $\mathbf{I}_{1j}$ for $G > 1$.

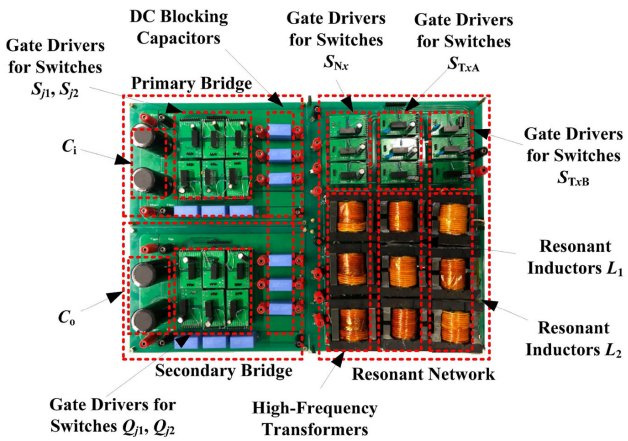

Fig. 14. Photograph of the constructed laboratory prototype of 1.5 kW.

3p-DABSRC. The output power for the tunable 3p-DABSRC is controlled by the impedance modulation method, where the impedance of the series LC network is modulated by varying ψ from 90° to 160°. Regarding the selection of the multiplier terms ϵ, σ, and κ, they are selected to limit the voltage stress across the SCC and keep a narrow range of frequency variation. The voltage stress across the SCC for the selected converter specifications is plotted using (35) and is shown in Fig. 16(b)

$$V_{\mathrm{C2,peak}} = \frac{\sqrt{2}I_{\mathrm{C2}}}{\omega C_{2t}} = \frac{\sqrt{2}(2\pi - 2\psi + \sin 2\psi)I_{\mathrm{C2}}}{\omega\pi C_2}. \quad (35)$$

The derivation of this expression can be found in [29].

To characterize the performance of the proposed converter, the constructed prototype has been extensively tested under both configurations, and its power conversion efficiency has been measured over a wide range of G (i.e., $0.5 \leq G \leq 1.5$). Moreover,

TABLE I
DESIGN SPECIFICATIONS OF THE PROPOSED 3p-DAB CONVERTER

Input voltage V_{in}	300 V
Nominal output voltage V_{o}	150 V
Output voltage range	75-225 V
Maximum output power $P_{\mathrm{o,max}}$	1500 W
Resonant inductor L_1	73.9 μH
Resonant inductor L_2	184.4 μH
Resonant capacitor C_1	81.5 nF
Resonant capacitor C_2	73.5 nF
Switching frequency f_{s} (3p-DABRIC)	35−50 kHz
Switching frequency f_{s} (3p-DABSRC)	46 kHz
Control angle of SCC ψ	90° − 160°
Transformer's Turns ratio n	2
Core Type	ETD-54 Core
Core Material	N87 Ferrite
Power gain ϵ	2.5
Frequency gain σ	1.4
Capacitance gain κ	56.7
MOSFETs	UJC06505K
Controller	TMS320F28379D

for better benchmarking its efficiency performance, the port currents and efficiency of the proposed converter have been compared to conventional 3p-DABRIC operating in UPF and ZVS modes and 3p-DABSRC under SPS modulation.

A. Experimental Results for Tunable 3p-DABRIC Under DFM Modulation

The prototype was operated as a tunable 3p-DABRIC from 40% to 100% of the rated output power with the proposed DFM

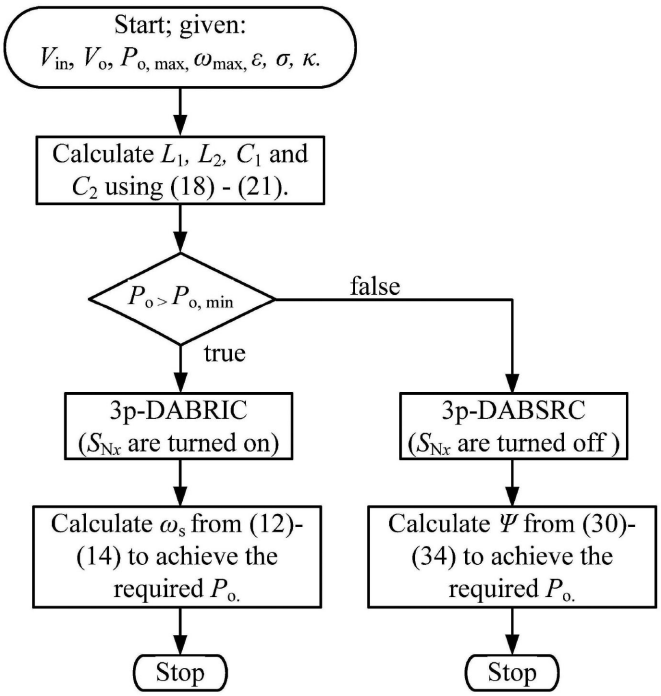

Fig. 15. Flowchart for design and operation of the proposed converter.

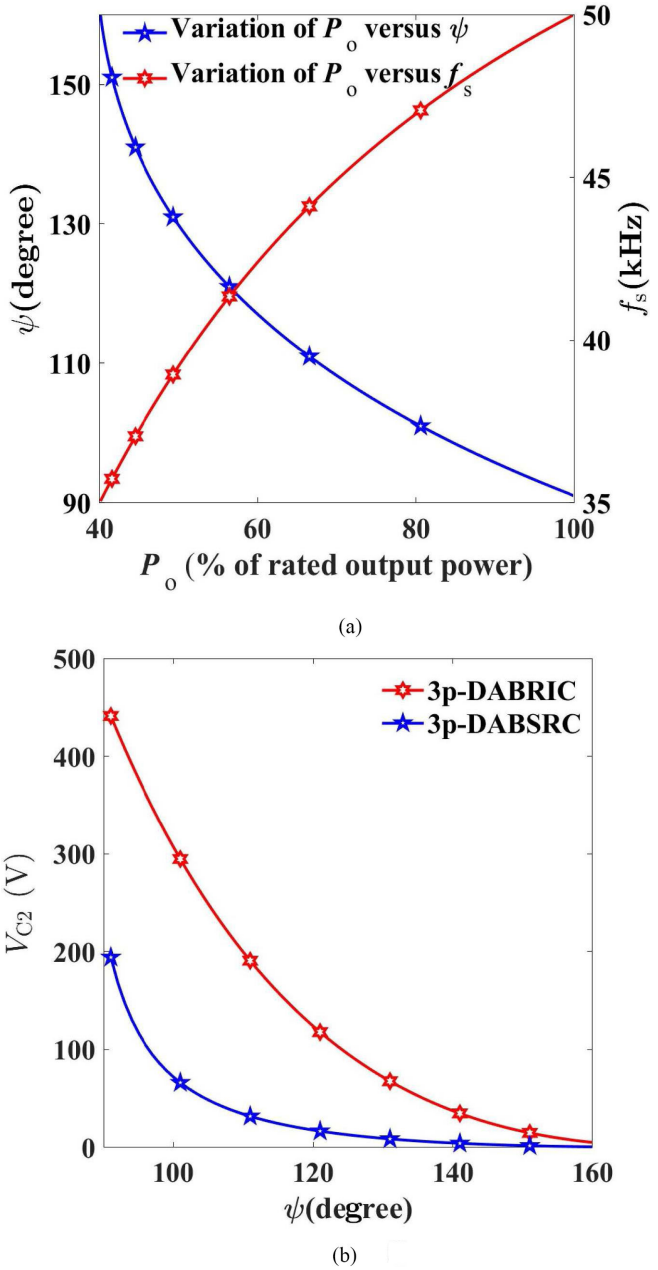

Fig. 16. (a) Variation of f_s and ψ versus P_o for the 3p-DABRIC. (b) Variation of V_{2t} versus ψ for the 3p-DABRIC and the 3p-DABSRC.

modulation, under which f_s and ψ were modulated simultaneously to maintain the immittance condition (i.e., $\omega_r = \omega_s$) throughout the entire power range. The corresponding experimental results are shown in Fig. 17 for three different power levels, i.e., 100%, 75%, and 50% of the rated output power. By inspection of the experimental waveforms shown in Fig. 17, it can be observed that v_{1j} and i_{1j} at the input ports [cf. Fig. 17(a), (c), and (e)] and v_{2j} and i_{2j} at the output ports [cf. Fig. 17(b), (d), and (f)] maintain an in-phase relationship for all the three output power levels. Moreover, it can also be observed that as the immittance condition is maintained under switching frequency variation, circulating current and reactive power are completely eliminated. The in-phase relationship between the current and voltage waveforms at all ports and the elimination of circulating current have led to significantly reduced rms port currents i_{1j} and i_{2j} and conduction loss. Furthermore, judging from the direction of i_{1j} and i_{2j} during the voltage transitions of v_{1j} and v_{2j}, it can be observed that all switches undergo ZVS commutation, leading to mitigation of switching loss. Overall, the elimination of circulating current and achievement of ZVS operation in all switches have contributed to the achievement of wide-range high-efficiency performance.

B. Experimental Results for Tunable 3p-DABSRC Under Impedance Modulation

Below 40% of the rated output power, the prototype was operated as a tunable 3p-DABSRC with impedance modulation. Under this modulation method, switching frequency f_s and phase shift θ were kept constant, and the output power was controlled by modulating the impedance of the series LC resonant network by means of varying the SCC control angle ψ. The corresponding experimental are shown in Fig. 18 corresponding to three different output power levels, i.e., 40%, 25%, and 10% of the rated output power. By inspection of Fig. 18, it can be observed that unlike SPS modulation where circulating current increases with the increase in θ, the proposed modulation method constantly operates the converter at the minimum tank current for the entire power range as θ is kept constant at the optimal value, as determined from (30), and ψ is used to modulate output power. Moreover, it can be observed from Fig. 18 that i_{1j} lags v_{1j} and leads v_{2j} leading to the ZVS operation of all switches. The waveforms depicting the ZVS operation of the primary-side switches S_{A1} and S_{A2} and secondary-side switches Q_{A1} and Q_{A2} are shown in Fig. 19(a) and (b), respectively, and the voltage

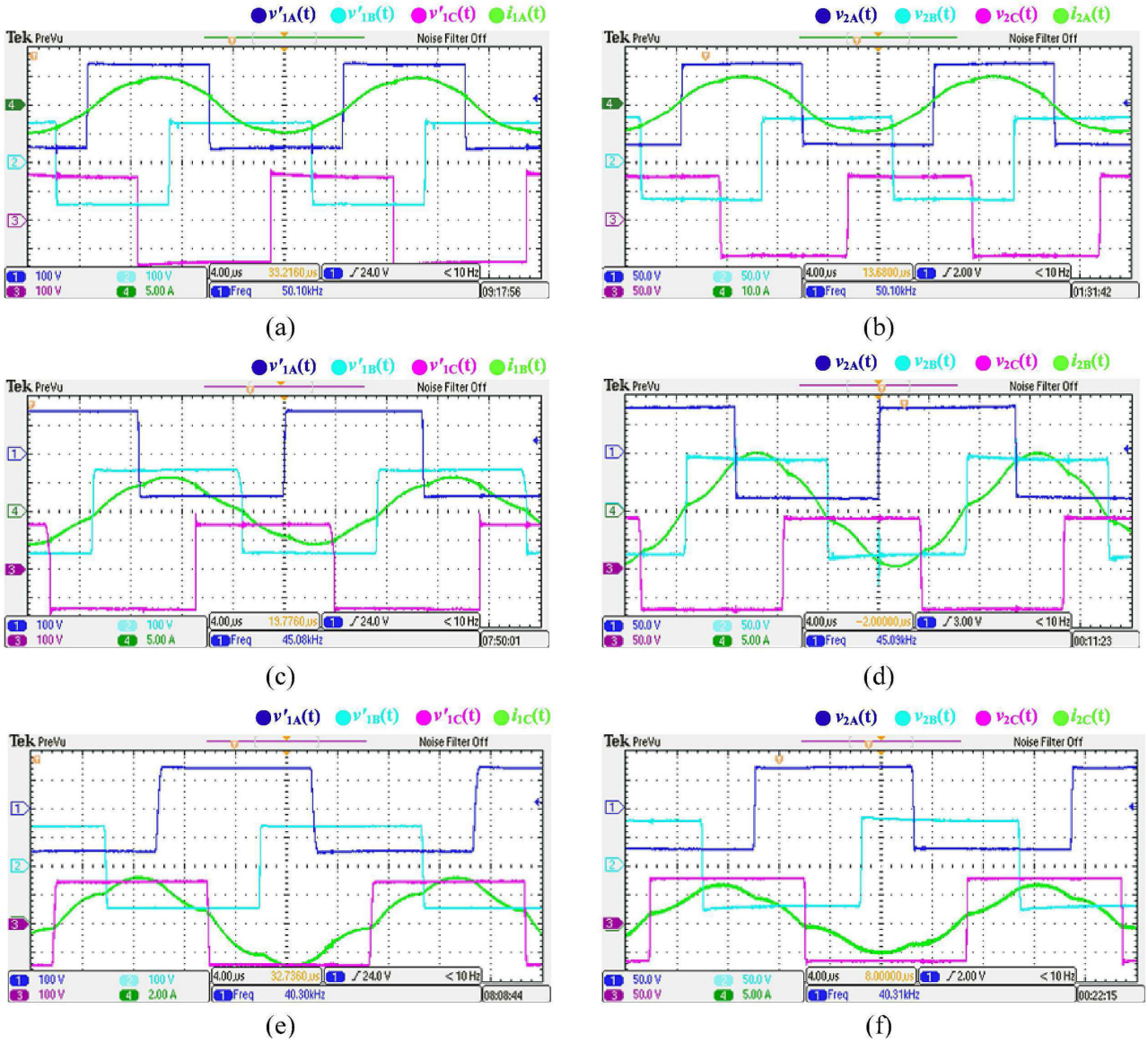

Fig. 17. Measured port voltages v'_{1j} and v_{2j} and currents i_{1j} and i_{2j} for the 3p-DABRIC under DFM at: (a) and (b) 100% of the rated output power with $f_s = 50$ kHz, and $\psi = 90°$; (c) and (d) 75% of the rated output power with $f_s = 45$ kHz, and $\psi = 104.7°$; and (e) and (f) 50% of the rated output power with $f_s = 40$ kHz, and $\psi = 123.9°$.

waveforms of the SCC are shown in Fig. 19(c). Hence, it can be concluded that under this operation mode, attenuation of the circulating current in conjunction with ZVS operation of all switches has contributed to the realization of high-efficiency performance at low-to-medium output power levels.

C. Closed-Loop Voltage-Mode Control Transient Performance Under Mode Switching

To demonstrate the transient performance of the proposed converter under fast load transitions and mode switching, the simulated closed-loop transient response of the proposed converter with voltage-mode control under step load changes of 1 A→7.5 A→1 A is shown in Fig. 20. The converter is designed to operate as a tunable 3p-DABSRC for load current below 4 A and a tunable 3p-DABRIC for load current above 4 A, the load current is sensed continuously, and mode transition occurs seamlessly as the load current exceeds/fall below the threshold value of 4 A. The block diagram representing the closed-loop voltage-mode control strategy of the proposed converter is depicted in Fig. 21. The feedback loop comprises a mode selection block, which selects between two different proportional–integral (PI) controllers (designed for each operation mode) on the basis of the load current and a compensation block that contains the two PI controllers that generate the appropriate control signals for output voltage regulation under each operation mode. A hysteresis band is designed in the mode selection block to reduce sensitivity at the threshold value of 4 A. Based on the simplified small-signal model of the proposed converter, as shown in Fig. 22, the PI controllers are designed with a crossover frequency of 500 Hz and a phase margin of 70°. The expressions for the small-signal value of the output current $\widetilde{i}_{o\_mode,avg}$ for

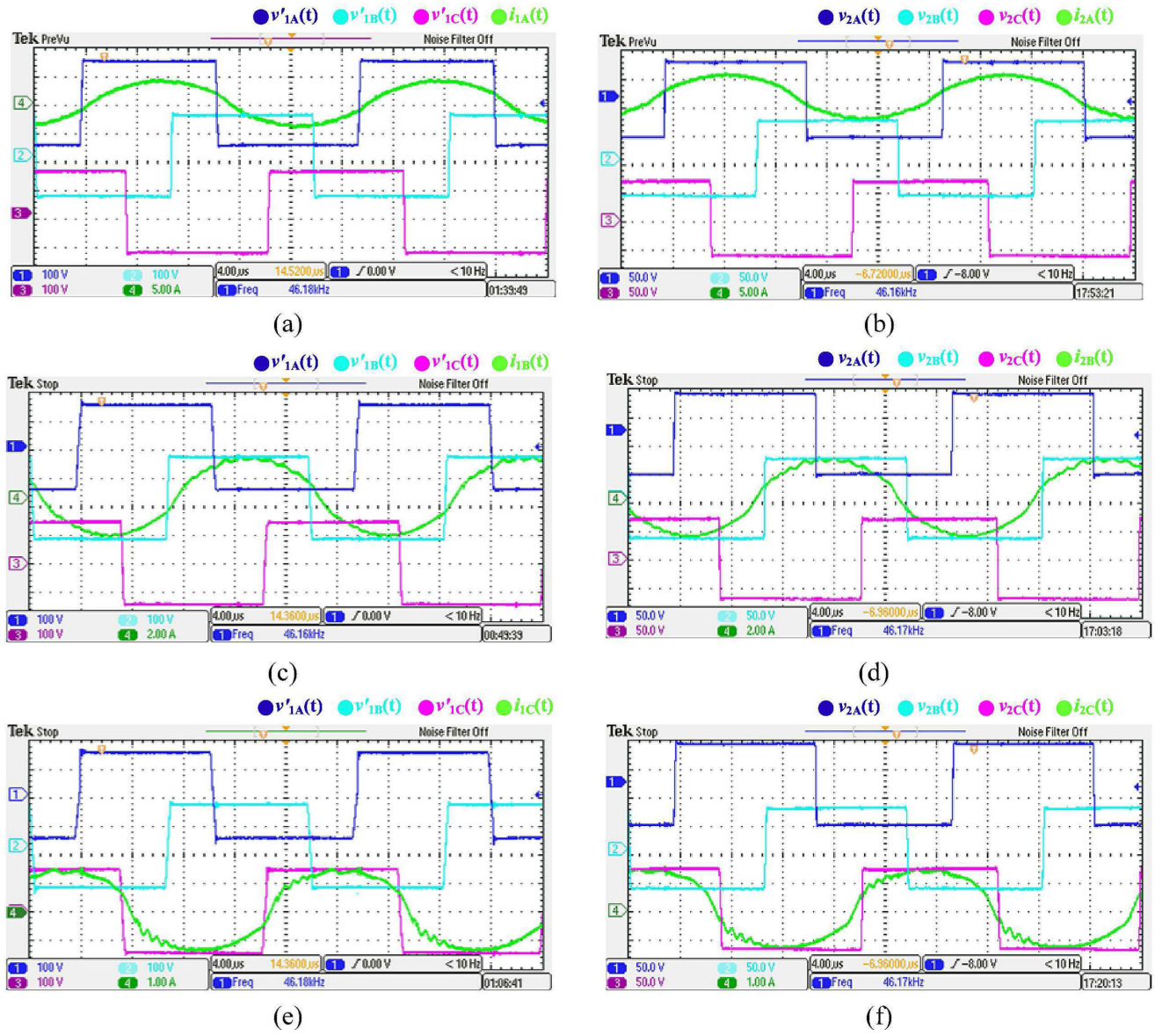

Fig. 18. Measured port voltages v'_{1j} and v_{2j} and currents i_{1j} and i_{2j} for the 3p-DABSRC under impedance modulation at: (a) and (b) 40% of the rated output power with $\psi = 90°$; (c) and (d) 25% of the rated output power with $\psi = 95.8°$; and (e) and (f) 10% of the rated output power with $\psi = 105.7°$.

the 3p-DABRIC and the 3p-DABSRC can be obtained by taking the partial derivative of (14) and (26) with respect to f_s and ψ, respectively. The resulting expressions are given by

$$\widetilde{i}_{o\_3p-DABRIC,avg} = \frac{12\sqrt{3}C_1V_{in}\left(4\pi^2C_1L_1f_s^2+1\right)}{n\pi\left(4\pi^2C_1L_1f_s^2-1\right)^2}\widetilde{f}_s \quad (36)$$

$$\widetilde{i}_{o\_3p-DABSRC,avg} = \frac{48C_2V_{in}f_s\sin(\theta)\left(\cos(\psi)^2-1\right)}{n\left(2\pi-4\pi^3C_2L_2f_s^2-2\psi+\sin(2\psi)\right)^2}\widetilde{\psi}. \quad (37)$$

For tunable 3p-DABRIC, as f_s is varied, the corresponding value of ψ required to maintain the immittance condition is taken from a lookup table. The Bode plots of the compensated loop gain for each operation mode are shown in Fig. 23. It can be seen from Figs. 20 and 23 that with suitably designed PI controllers, the converter's output voltage is well regulated during fast load transients, and the converter is able to operate stably during mode transition.

D. Performance Comparison With Conventional 3p-DABRIC and 3p-DABSRC

To demonstrate the merits of the proposed topology and modulation schemes, the performance of the proposed converter was evaluated and compared (in terms of rms port currents, ZVS range, and power conversion efficiency) with the conventional 3p-DABRIC and 3p-DABSRC with fixed resonant networks. The conventional 3p-DABRIC with a fixed immittance network operating with UPF and full-range ZVS modes and 3p-DABSRC operating with SPS modulation were included in the comparison. For a more comprehensive comparison, wide-range variations in G (i.e., $0.5 \leq G \leq 1.5$) are considered. The simulated

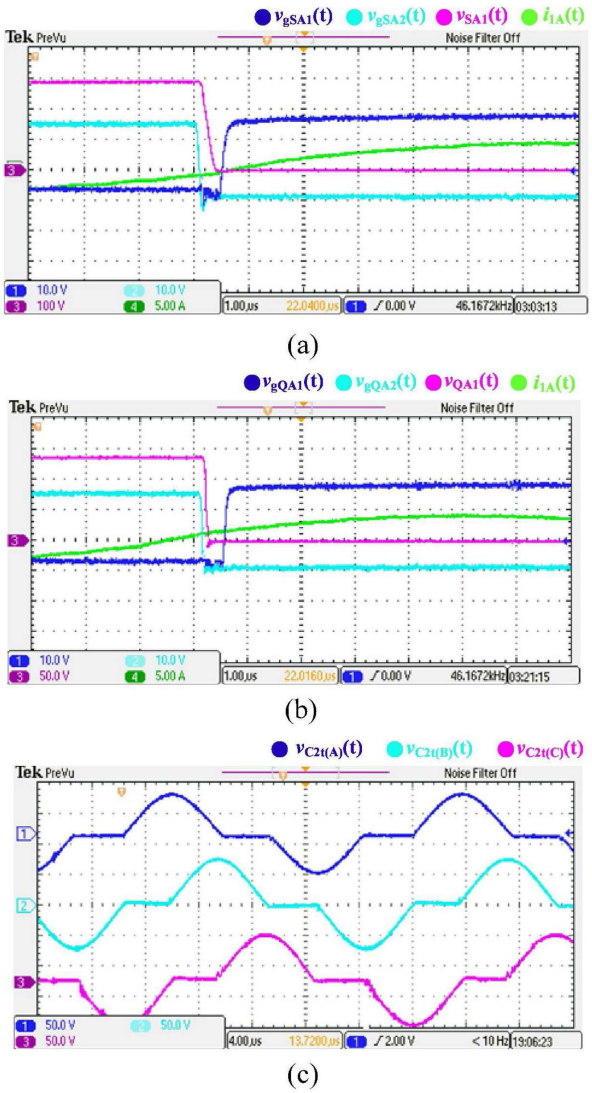

Fig. 19. (a) ZVS operation of S_{A1} and S_{A2}. (b) ZVS operation of Q_{A1} and Q_{A2}. (c) Measured waveforms of $v_{2Ct(A)}$, $v_{2Ct(B)}$, and $v_{2Ct(C)}$ at $\psi = 115.3°$.

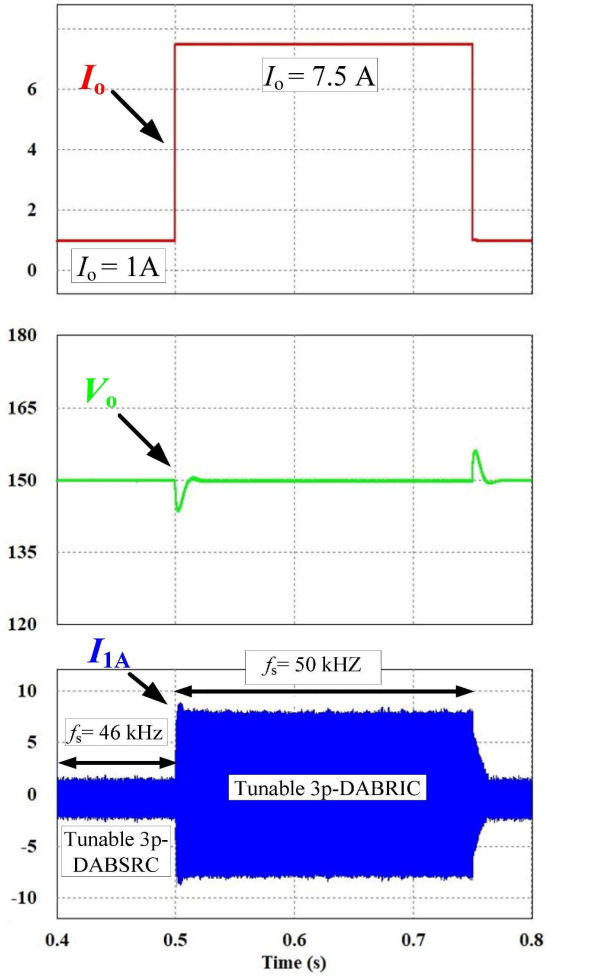

Fig. 20. Closed-loop transient response under step load changes of 1 A→7.5 A→1 A accompanied by mode transitions between the 3p-DABSRC and the 3p-DABRIC.

rms port currents (i.e., $\mathbf{I}_{N,rms} = (\mathbf{I}_{1j}+\mathbf{I}_{2j})/2$) of the proposed converter, conventional 3p-DABRIC, and 3p-DABSRC for the selected converter specifications are plotted in Fig. 24(a)–(c) for $G = 0.5$, $G = 1$, and $G = 1.5$, respectively. By inspection of Fig. 24(a)–(c), it can be observed that the proposed converter offers significantly lower rms port currents under wide-range variations in G as compared to the other two topologies. The lower rms port currents of the proposed converter are attributed to the achievement of wide-range zero circulating current, which favorably leads to lower conduction loss. Moreover, as the proposed converter is capable of achieving full-range ZVS operation for all switches irrespective of variations in G, the proposed converter incurs lower switching loss in comparison to the other two topologies. The ZVS range comparison of the proposed converter with the other two topologies is presented in Fig. 25. It can be seen from Fig. 25 that unlike UPF operation of 3p-DABRIC (cf. Fig. 25(a), where switches S_{j3} and S_{j4} are hard-switched) and SPS operation of 3p-DABSRC (cf. Fig. 25(b), where switches Q_{j1} and Q_{j2} are hard-switched for $G < 1$ and switches S_{j1}, S_{j2} are hard-switched for $G > 1$), the proposed converter achieves ZVS operation for all the switches independent of output power level and input-to-output voltage ratio [cf. Fig. 25(c)].

The measured power conversion efficiency of the proposed converter, conventional 3p-DABRIC, and 3p-DABSRC are plotted in Fig. 26(a)–(c) for $G = 0.5$, $G = 1$, and $G = 1.5$, respectively. It can be observed from Fig. 26(a) and (c) that due to reconfiguration flexibility, attenuation of circulating current, and full-range ZVS operation, the proposed converter offers a wide-range high-efficiency performance as compared to the other two topologies. For the conventional 3p-DABSRC, it achieved a better efficiency performance at low-to-medium output power levels for $G = 1$ but suffered from high circulating current and hard-switching under $G \neq 1$ leading to a deterioration of efficiency performance. For the conventional 3p-DABRIC operating with UPF, 33% of the switches suffered from hard switching and high circulating current prevails under light-load condition. The worst efficiency performance resulted from the conventional 3p-DABRIC operating with full-range ZVS mode

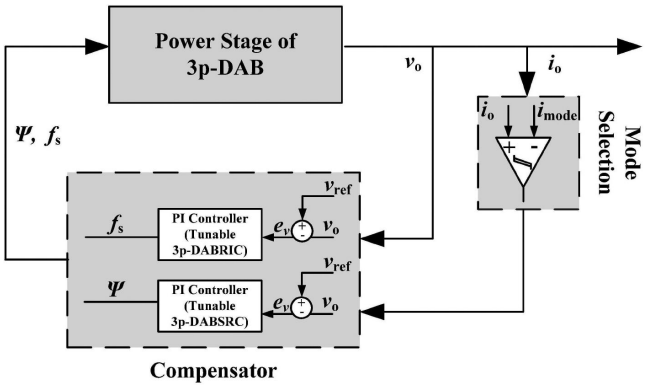

Fig. 21. Block diagram of the closed-loop implementation of the proposed converter.

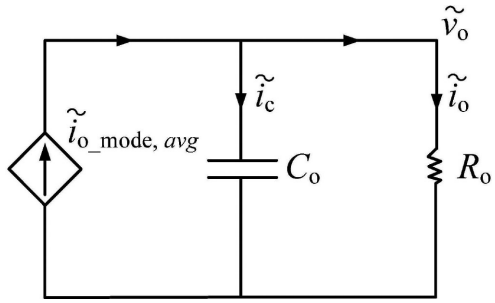

Fig. 22. Simplified small-signal model of the proposed converter.

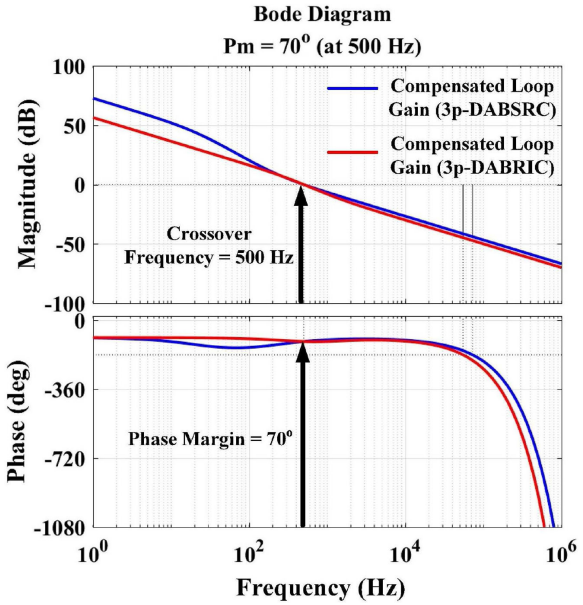

Fig. 23. Bode plots of the compensated loop gain for each operation mode.

due to excessive conduction loss caused by the high circulating current needed to realize the ZVS operation. For the proposed converter, switching loss is negligible due to full-range ZVS operation of all switches, and the dominant loss mechanism is conduction loss. The increase in conduction loss with increasing load leads to a decrease in efficiency. However, due to wide-range zero circulating current, UPF operation, and ZVS operation of all switches, the loss in efficiency with increasing load is quite small, and the proposed converter offers relatively flat (i.e., weak dependence on load) efficiency curves as compared to the other two topologies.

E. Power Loss Model

The power loss breakdown of the proposed converter for both operation modes over wide output voltage and power range has been calculated by adopting and extending the power loss models proposed in [31] and [32]. The developed power loss model [cf. (38)] considers the following losses:

$$P_{\mathrm{L}} = P_{\mathrm{Cond}} + P_{\mathrm{SCC}} + P_{\mathrm{Core}} + P_{\mathrm{Sw}}. \tag{38}$$

1) Conduction Loss: The conduction loss P_{Cond} is calculated using (39) and is contributed by the ON-state resistances $R_{\mathrm{ON,p}}$ and $R_{\mathrm{ON,s}}$ of the MOSFETs in the primary and secondary bridges, respectively, ac resistances R_{L1} and R_{L2} of the resonant inductors L_1 and L_2, respectively, and ac resistance R_{T} (secondary-reflected) of the HF transformer windings

$$P_{\mathrm{cond}} = 6 \times \left(\left(\frac{I_{1\mathrm{j,rms}}}{n\sqrt{2}} \right)^2 R_{\mathrm{ON,p}} + \left(\frac{I_{2\mathrm{j,rms}}}{\sqrt{2}} \right)^2 R_{\mathrm{ON,s}} \right) + 3 \times \left(\left(I_{\mathrm{L1,rms}}\right)^2 R_{\mathrm{L1}} + \left(I_{\mathrm{L2,rms}}\right)^2 R_{\mathrm{L2}} + \left(I_{2\mathrm{j,rms}}\right)^2 R_{\mathrm{T}} \right). \tag{39}$$

2) Power Loss in SCC: The power loss in the SCC is calculated using (40) and is contributed by the ON-state resistance $R_{\mathrm{ON,SCC}}$ of the SCC MOSFETs and the forward voltage drop V_f of the SCC body diodes [29]

$$P_{\mathrm{SCC}} = 3 \times \left(\left(I_{\mathrm{SCC,rms}}\right)^2 R_{\mathrm{ON,SCC}} + V_f I_{\mathrm{SCC,rms}} \right). \tag{40}$$

3) Core Loss: The total core loss incurred in the resonant inductors L_1 and L_2 and HF transformers is calculated by applying the modified Steinmetz equation as

$$P_{\mathrm{core}} = 3 \times \left(K_{fe} A_c l_m \left(\Delta B_{\mathrm{T}}^{\beta} + \Delta B_{L1}^{\beta} + \Delta B_{L2}^{\beta} \right) \right) \tag{41}$$

where K_{fe}, $A_c l_m$, and β are the loss coefficient, volume, and loss exponent of the magnetic core, respectively, while ΔB_T, ΔB_{L1}, and ΔB_{L2} are the flux densities of the HF transformer, resonant inductor L_1, and resonant inductor L_2, respectively.

4) Switching Loss: The total switching loss is given by (42) and is caused by the voltage and current overlap during the switching transitions of MOSFETs

$$P_{\mathrm{Sw}} = \left(6 \times \left| \frac{i_{1j}(0)}{n} \right| V'_{1j} \left(t_{\mathrm{rip}} + t_{\mathrm{rvp}} + t_{\mathrm{fip}} + t_{\mathrm{rvp}} \right) f_{\mathrm{s}} \right) + \left(6 \times \left| i_{2j}(\theta) \right| V_{2j} \left(t_{\mathrm{ris}} + t_{\mathrm{rvs}} + t_{\mathrm{fis}} + t_{\mathrm{rvs}} \right) f_{\mathrm{s}} \right) \tag{42}$$

where $|\frac{i_{1j}(0)}{n}|$ and $|i_{2j}(\theta)|$ are the instantaneous current values at the turn-ON instants of primary- and secondary-bridge MOSFETs; t_{rip}, t_{rvp}, t_{fip}, and t_{rvp} are the rise and fall time of the current and voltage of the primary-bridge MOSFETs, while t_{ris}, t_{rvs}, t_{fis}, and t_{rvs} are the same for secondary-bridge MOSFETs.

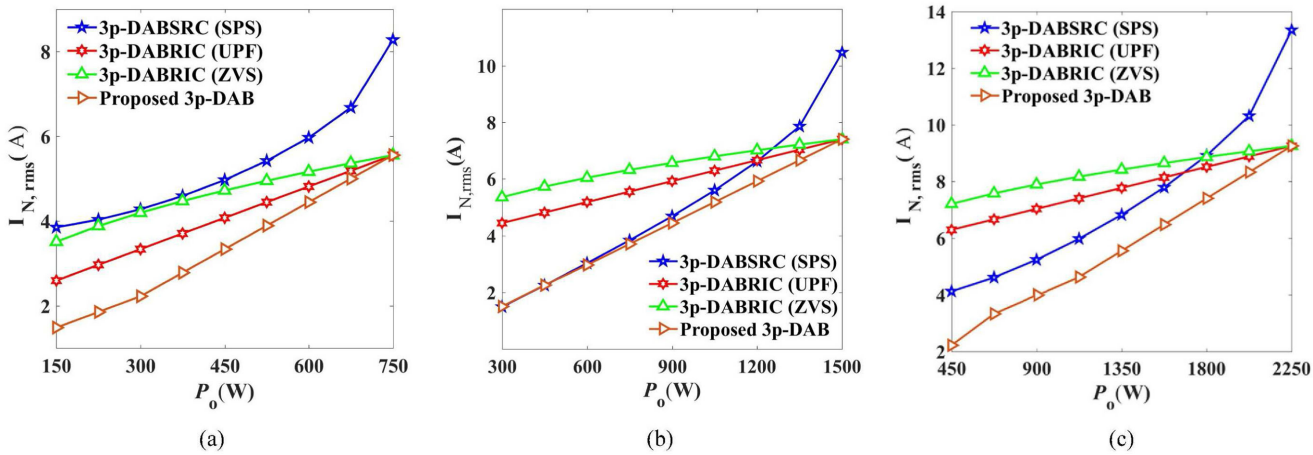

Fig. 24. Normalized simulated port currents $I_{\mathrm{N,rms}}$ comparison between the proposed converter and the conventional 3p-DABRIC (UPF and ZVS modes) and 3p-DABSRC (SPS modulation) for (a) $G = 0.5$, (b) $G = 1$, and (c) $G = 1.5$.

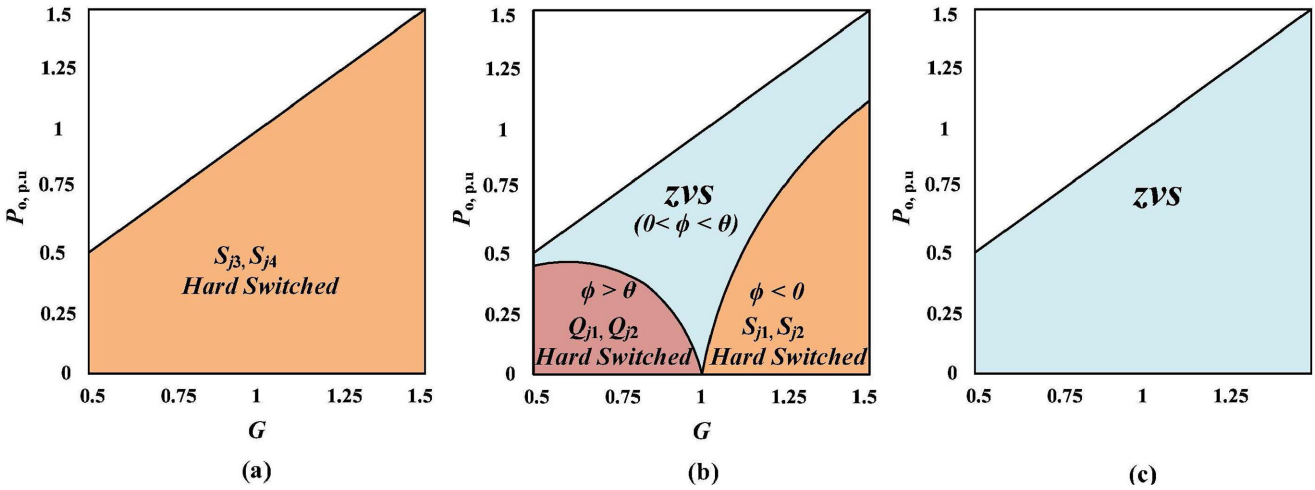

Fig. 25. (a) ZVS range of 3p-DABRIC (UPF mode). (b) ZVS range of the SPS-controlled 3p-DABSRC. (c) ZVS range of the proposed converter.

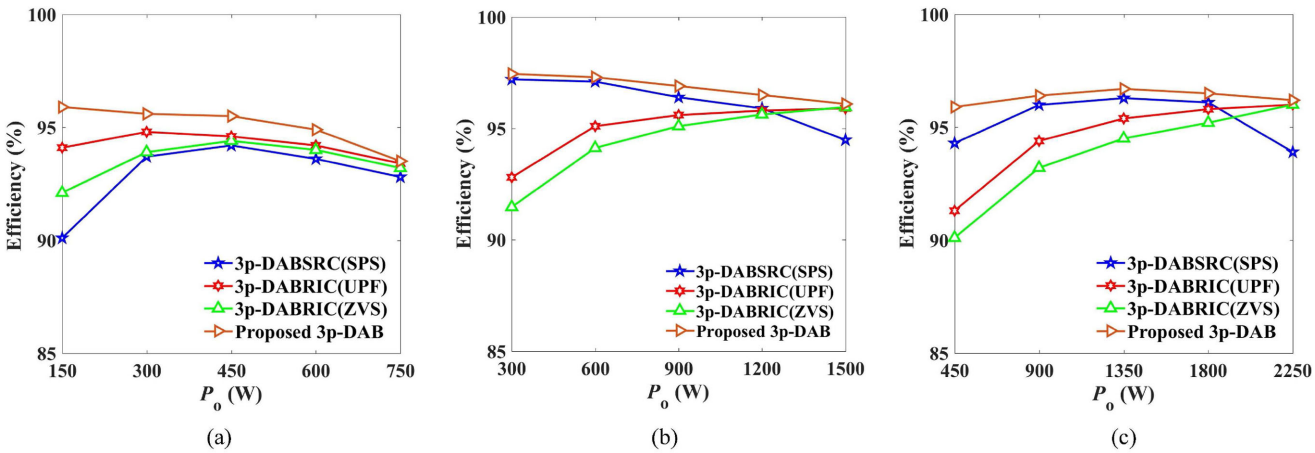

Fig. 26. Comparison of the measured power conversion efficiency between the proposed converter and the conventional 3p-DABRIC (UPF and ZVS modes) and 3p-DABSRC (SPS modulation) for (a) $G = 0.5$, (b) $G = 1$, and (c) $G = 1.5$.

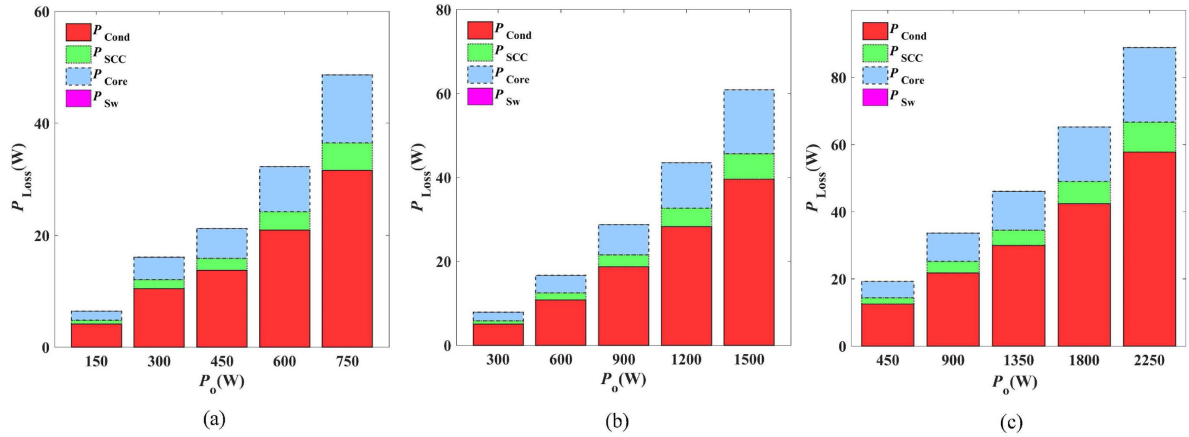

Fig. 27. Power loss breakdown of the proposed converter for (a) $G = 0.5$, (b) $G = 1$, and (c) $G = 1.5$.

TABLE II
COMPARISON BETWEEN THE PROPOSED AND EXISTING TOPOLOGIES

S. No.	Ref	No. of Switches	Additional Resonant Components	Full-Range ZVS	Unity Power Factor Operation	Zero Circulating Current	Zero Backflow Power	Minimum Tank Current
1	[11]–[13]	24	0	✓	X	X	X	X
2	[15], [16]	21	0	✓	X	X	X	X
3	[19], [20]	12	9	✓	X	X	X	X
4	[21]	18	12	X	✓	X	✓	X
5	[26]	21	12	✓	✓	X	✓	X
6	Proposed Topology	21	12	✓	✓	✓	✓	✓

By using (38)–(42), the power loss breakdown of the proposed converter is calculated and shown in Fig. 27(a)–(c) for $G = 0.5$, $G = 1$, and $G = 1.5$, respectively. Since ZVS operation is achieved for the entire operating range, the switching loss P_{Sw} of the MOSFETs in the primary and secondary bridges is negligible and is not shown in Fig. 27. It can be seen from Fig. 27 that the major source of power loss of the proposed converter is attributed to conduction loss for the entire operating range.

Finally, a comprehensive comparison of the proposed 3p-DAB topology with the existing 3p-DAB topologies is presented in Table II to conclude this article.

VII. CONCLUSION

A flexible and reconfigurable topology of a three-phase DAB converter utilizing an RTRN has been proposed in this article. The proposed converter offers multiple DoFs in terms of the availability of multiple control parameters and topological variations to achieve wide-range high-efficiency performance. The proposed converter has been designed to switch between two different network configurations that are controlled with two different modulation schemes to optimize its efficiency performance in both low- and medium-to-high power operation. For medium-to-high output power levels, the converter operates as a tunable 3p-DABRIC with DFM modulation. Under this mode of operation, the converter's output power is modulated by synchronously varying the resonance frequency of the immittance network and the switching frequency by using an SCC. For low-to-medium output power levels, the converter operates as a tunable 3p-DAB SRC with impedance modulation. Under this mode of operation, the converter's output power is modulated by varying the impedance of a series LC resonant network with the aid of SCC while keeping the switching frequency and phase shift constant. The combination of both operation modes has led to the realization of wide-range zero circulating current and full-range ZVS operation of all switches for a wide range of output power and input-to-output voltage ratio. The presented theoretical analysis has been validated by the experimental results obtained from a 1.5-kW laboratory prototype yielding wide-range high-efficiency performance.

REFERENCES

[1] R. W. De Doncker, D. M. Divan, and M. H. K. Kheraluwala, "A three-phase soft-switched high-power-density DC/DC converter for high-power applications," *IEEE Trans. Ind. Appl.*, vol. 27, no. 1, pp. 63–73, Jan./Feb. 1991.

[2] Z. Wang, S. Member, H. Li, and S. Member, "A soft switching three-phase current-fed bidirectional dc-dc converter with high efficiency over a wide input voltage range," *IEEE Trans. Power Electron.*, vol. 27, no. 2, pp. 669–684, Feb. 2012.

[3] J. Huang, Y. Wang, Z. Li, Y. Jiang, and W. Lei, "Simultaneous PWM control to operate the three-phase dual active bridge converter under soft switching in the whole load range," in *Proc. Conf. IEEE Appl. Power Electron. Conf. Expo.*, 2015, pp. 2885–2891.

[4] J. Hu, Z. Yang, N. Soltau, and R. W. De Doncker, "A duty-cycle control method to ensure soft-switching operation of a high-power three-phase dual-active bridge converter," in *Proc. IEEE 3rd Int. Future Energy Electron. Conf. ECCE Asia*, 2017, pp. 1–6.

[5] H.-J. Choi, H.-P. Park, M.-A. Kim, C. Sang-Gyu, C.-U. Lee, and J.-H. Jung, "Modulation strategy of three-phase dual-active-bridge converter using SiC-MOSFET for improving light load condition," in *Proc. IEEE Workshop Wide Bandgap Power Devices Appl. Asia*, 2019, pp. 1–5.

[6] N. A. Dung, H. J. Chiu, J. Y. Lin, Y. C. Hsieh, H. T. Chen, and B. X. Zeng, "Novel modulation of isolated bidirectional DC-DC converter for energy storage systems," *IEEE Trans. Power Electron.*, vol. 34, no. 2, pp. 1266–1275, Feb. 2019.

[7] J. Hiltunen and V. Vesa, "Variable-frequency phase shift modulation of a dual active bridge converter," *IEEE Trans. Power Electron.*, vol. 30, no. 12, pp. 7138–7148, Dec. 2015.

[8] Z. Li, Y. Wang, L. Shi, J. Huang, and W. Lei, "Optimized modulation strategy for three-phase dual-active-bridge DC-DC converters to minimize rms inductor current in the whole load range," in *Proc. IEEE 8th Int. Power Electron. Motion Control Conf.*, 2016, pp. 2787–2791.

[9] J. Hu, N. Soltau, and R. W. De Doncker, "Asymmetrical duty-cycle control of three-phase dual-active bridge converter for soft-switching range extension," in *Proc. Energy Convers. Congr. Expo.*, 2016, pp. 1–8.

[10] J. Huang, Z. Li, L. Shi, Y. Wang, and J. Zhu, "Optimized modulation and dynamic control of a three-phase dual active bridge converter with variable duty cycles," *IEEE Trans. Power Electron.*, vol. 34, no. 3, pp. 2856–2873, Mar. 2019.

[11] N. H. Baars, C. G. Wijnands, and J. Everts, "A three-level three-phase dual active bridge DC-DC converter with a star-delta connected transformer," in *Proc. IEEE Veh. Power Propulsion Conf.*, 2016, pp. 1–6.

[12] N. H. Baars, J. Everts, C. G. E. Wijnands, and E. A. Lomonova, "Evaluation of a high-power three-phase dual active bridge DC-DC converter with three-level phase-legs," in *Proc. 18th Eur. Conf. Power Electron. Appl.*, 2016, pp. 1–10.

[13] N. H. Baars, C. G. Wijnands, and J. Everts, "ZVS modulation strategy for a three-phase dual active bridge DC-DC converter with three-level phase-legs," in *Proc. 18th Eur. Conf. Power Electron. Appl.*, 2016, pp. 1–10.

[14] B. Jin and X. Yuan, "Topology, efficiency analysis, and control of a four-level π -type converter," *IEEE Trans. Emerg. Sel. Topics Power Electron.*, vol. 7, no. 2, pp. 1044–1059, Jun. 2019.

[15] H. M. De Oliveira Filho, D. D. S. Oliveira, and P. P. Praça, "Steady-state analysis of a ZVS bidirectional isolated three-phase DC-DC converter using dual phase-shift control with variable duty cycle," *IEEE Trans. Power Electron.*, vol. 31, no. 3, pp. 1863–1872, Mar. 2016.

[16] G. Waltrich, M. A. M. Hendrix, and J. L. Duarte, "Three-phase bidirectional DC/DC converter with six inverter legs in parallel for EV applications," *IEEE Trans. Ind. Electron.*, vol. 63, no. 3, pp. 1372–1384, Mar. 2016.

[17] R. N. Oliveira, L. Mazza, H. O. Filho, and D. de Souza Oliveira, "A three-port isolated three-phase current-fed DC-DC converter feasible to PV and storage energy system connection on a dc distribution grid," *IEEE Trans. Ind. Appl.*, vol. 55, no. 5, pp. 4910–4919, Sep./Oct. 2019.

[18] J. Voss and R. W. De Doncker, "Modified auxiliary-resonant commutated pole applied in a three-phase dual-active bridge DC/DC converter," *IEEE Trans. Power Electron.*, vol. 35, no. 2, pp. 1256–1268, Feb. 2020.

[19] A. N. Rahman, C. Y. Lee, H. J. Chiu, and Y. C. Hsieh, "Bidirectional three-phase LLC resonant converter," in *Proc. ITEC Asia-Pacific IEEE Transp. Electrif. Conf. Expo./Asia-Pacific: E-Mobility: A Journey Now Beyond*, 2018, pp. 1–5.

[20] M. Noah *et al.*, "Magnetic design and experimental evaluation of a commercially available single integrated transformer in three-phase LLC resonant converter," *IEEE Trans. Ind. Appl.*, vol. 54, no. 6, pp. 6190–6204, Nov./Dec. 2018.

[21] A. Z. Khan, K. H. Loo, and Y. M. Lai, "Design, analysis and performance characterization of dual-active-bridge DC-DC converter utilizing three-phase resonant immittance network," *IEEE Trans. Power Electron.*, vol. 34, no. 2, pp. 1159–1180, Feb. 2019.

[22] A. K. Bhat and R. L. Zheng, "Analysis and design of a three-phase LCC-type resonant converter," *IEEE Trans. Aerosp. Electron. Syst.*, vol. 34, no. 2, pp. 508–519, Apr. 1998.

[23] A. Z. Khan and K. H. Loo, "A three-phase dual-active-bridge DC-DC immittance converter," in *Proc. IEEE Energy Convers. Congr. Exp.*, 2018, pp. 6336–6343.

[24] H. Irie and S. Oohashi, "A three-phase constant-current source using an immittance converter," *Elect. Eng. Jpn.*, vol. 151, no. 4, pp. 47–54, 2005.

[25] H. Irie and T. Nishisako, "Three-phase immittance converter," *Elect. Eng. Jpn.*, vol. 145, no. 1, pp. 52–58, 2003.

[26] A. Z. Khan and K. H. Loo, "A three-phase dual-active-bridge dc-dc converter with reconfigurable resonant network for efficient wide voltage range operation," *IEEE Trans. Power Electron.*, vol. 35, no. 2, pp. 1322–1339, Feb. 2020.

[27] R. Mirzahosseini and F. Tahami, "A phase-shift three-phase bidirectional series resonant DC/DC converter," in *Proc. 37th Annu. Conf. IEEE Ind. Electron. Soc.*, 2011, pp. 1137–1143.

[28] A. Z. Khan and K. H. Loo, "A reconfigurable three-phase dual-active-bridge DC-DC converter designed for wide-range high-efficiency operation," in *Proc. IEEE 10th Int. Symp. Power Electron. Distrib. Gener. Syst.*, 2019, pp. 147–154.

[29] M. Yaqoob, K. H. Loo, and Y. M. Lai, "Fully soft-switched dual-active-bridge converter with switched-impedance-based power control," *IEEE Trans. Power Electron.*, vol. 33, no. 11, pp. 9267–9281, Nov. 2018.

[30] W. J. Gu and K. Harada, "A new method to regulate resonant converters," *IEEE Trans. Power Electron.*, vol. 3, no. 4, pp. 430–439, Oct. 1988.

[31] F. Krismer and J. W. Kolar, "Accurate power loss model derivation of a high-current dual active bridge converter for an automotive application," *IEEE Trans. Ind. Electron.*, vol. 57, no. 3, pp. 881–891, Mar. 2010.

[32] M. Yaqoob, K. H. Loo, Y. P. Chan, and J. Jatskevich, "Optimal modulation for a fifth-order dual-active-bridge resonant immittance DC-DC converter," *IEEE Trans. Power Electron.*, vol. 35, no. 1, pp. 70–82, Jan. 2020.

Akif Zia Khan (Student Member, IEEE) received the B.Eng. degree in electrical engineering from the National University of Sciences and Technology (NUST), Islamabad, Pakistan, in 2011, the M.Sc. degree in electric power systems from the North China Electric Power University, Beijing, China, in 2014, and the Ph.D. degree in power electronics from the Hong Kong Polytechnic University, Hung Hom, Hong Kong, in 2020.

From 2014 to 2016, he was a Lecturer with the U.S.–Pakistan Center for Advanced Studies in Energy, NUST. During the Spring of 2016, he was a Visiting Research Scholar with the Power Systems Engineering Research Center, Arizona State University, Tempe, AZ, USA. During 2019, he was a Visiting Ph.D. Scholar with the Center of Reliable Power Electronics, Department of Energy Technology, Aalborg University, Aalborg, Denmark. He is currently a Lecturer at the U.S.–Pakistan Center for Advanced Studies in Energy, NUST.

Dr. Khan contributes regularly as a reviewer for various international journals and conferences. His current research interests include design, modeling, and control of high-power and high-frequency bidirectional resonant power converters for various power processing applications.

Yiu Pang Chan (Student Member, IEEE) received the B.Sc. (hons.) degree in engineering physics in 2015 from Hong Kong Polytechnic University, Hung Hom, Hong Kong, where he is currently working toward the Ph.D. degree in power electronics.

His research interests include high-frequency bidirectional isolated dc–dc and ac–dc converters.

Muhammad Yaqoob (Member, IEEE) received the B.Eng. degree in electronics engineering from the National University of Sciences and Technology, Islamabad, Pakistan, in 2012, and the Ph.D. degree in power electronics from The Hong Kong Polytechnic University, Hung Hom, Hong Kong, in 2018.

He is currently a Senior Power Electronics Engineer with the Huawei Research Center, Stockholm, Sweden. His current research interests include high-frequency bidirectional isolated dc–dc and ac–dc converters for electric vehicle applications.

Dr. Yaqoob is a Reviewer for the IEEE TRANSACTIONS ON POWER ELECTRONICS and the IEEE TRANSACTIONS ON INDUSTRIAL ELECTRONICS.

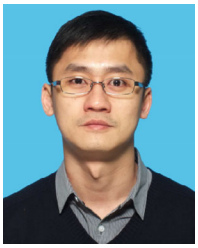

Ka-Hong Loo (Member, IEEE) received the B.Eng. (hons.) degree in electronic engineering and the Ph.D. degree from the University of Sheffield, Sheffield, U.K., in 1999 and 2002, respectively.

Upon completion of his doctoral degree, he received the Japan Society for the Promotion of Science Postdoctoral Fellowship and worked as a Postdoctoral Researcher with Ehime University, Matsuyama, Japan, from 2002 to 2004. In 2006, he joined The Hong Kong Polytechnic University, Hung Hom, Hong Kong, where he is currently an Associate Professor with the Department of Electronic and Information Engineering. His research interests include high-frequency power conversion, in particular power converters for renewable energy systems.

Dr. Loo has been an Associate Editor for the IEEE TRANSACTIONS ON ENERGY CONVERSION since 2013 and the IEEE POWER ENGINEERING LETTERS since 2015. He contributes regularly as a reviewer for various international journals and conferences. He is currently the Chair of the Power Electronics and Control Subcommittee of the IEEE Technical Committee on Transportation Electrification.

Pooya Davari (Senior Member, IEEE) received the B.Sc. and M.Sc. degrees in electronic engineering from University of Mazandaran, Babol, Iran, in 2004 and 2008, respectively, and the Ph.D. degree in power electronics from the Queensland University of Technology (QUT), Brisbane, QLD, Australia, in 2013.

From 2005 to 2010, he was involved in several electronics and power electronics projects, as a Development Engineer. From 2013 to 2014, he was a Lecturer with QUT. He joined as a Postdoctoral Researcher with Aalborg University, Aalborg, Denmark, in 2014, where he is currently an Associate Professor. He has been focusing on electromagnetic interference (EMI), power quality, and harmonic mitigation analysis, and control in power electronic systems. He has authored or coauthored more than 140 technical papers.

Dr. Davari is the recipient of a research grant from the Danish Council of Independent Research (DFF-FTP) in 2016 and the 2020 IEEE Electromagnetic Compatibility Society Young Professional Award for his contribution to EMI and harmonic mitigation and modeling in power electronic applications. He was a Guest Associate Editor for the *IET Journal of Power Electronics*, the IEEE ACCESS, the *Journal of Electronics, and the Journal of Applied Sciences*. He is an Associate Editor for the *Journal of Power Electronics* and the *IET Electronics*, and the Editorial Board Member for the *EPE Journal* and the *Journal of Applied Sciences*. He is member of the International Scientific Committee of EPE (Energy Conversion Congress and Exhibition Europe) and a member of Joint Working Group 6 and Working Group 8 at the IEC standardization TC77A.

Frede Blaabjerg (Fellow, IEEE) received the Ph.D. degree in electrical engineering from Aalborg University, Aalborg, Denmark, in 1995.

From 1987 to 1988, he was with ABB-Scandia, Randers, Denmark. He became an Assistant Professor in 1992, an Associate Professor in 1996, and a Full Professor of power electronics and drives in 1998 with Aalborg University. In 2017, he became a Villum Investigator. He is honoris causa with the University Politehnica Timisoara, Timişoara, Romania and Tallinn Technical University, Tallinn, Estonia. He has authored or coauthored more than 600 journal papers in the field of power electronics and its applications. He is the co-author of four monographs and editor of ten books in power electronics and its applications. His current research interests include power electronics and its applications such as in wind turbines, photovoltaic systems, reliability, harmonics, and adjustable-speed drives.

Dr. Blaabjerg has received 32 IEEE Prize Paper Awards, the IEEE Power Electronics Society Distinguished Service Award in 2009, the EPE-PEMC Council Award in 2010, the IEEE William E. Newell Power Electronics Award 2014, the Villum Kann Rasmussen Research Award 2014, the Global Energy Prize in 2019, and the 2020 IEEE Edison Medal. He was the Editor-in-Chief of the IEEE TRANSACTIONS ON POWER ELECTRONICS from 2006 to 2012. He was a Distinguished Lecturer for the IEEE Power Electronics Society from 2005 to 2007 and the IEEE Industry Applications Society from 2010 to 2011 as well as from 2017 to 2018. For 2019–2020, he is the President of the IEEE Power Electronics Society. He is also the Vice-President of the Danish Academy of Technical Sciences. He is nominated in 2014–2019 by Thomson Reuters to be between the 250 most-cited researchers in engineering in the world.